materials

MDPI

Article

Effect of the Sulfate-to-Chloride Concentration Ratio on the Destabilization of the Passive Film on HRB400 Reinforcing Steel in Simulated Concrete Pore Solution

Mingtao Liu [1,*], Yang Yi [1], Cailong Ma [1,2,*] and Xiangjun Niu [3]

[1] School of Civil Engineering and Architecture, Xinjiang University, Urumqi 830046, China; yiyang23333@gmail.com
[2] Xinjiang Key Laboratory of Building Structure and Earthquake Resistance, Xinjiang University, Urumqi 830046, China
[3] Xinjiang Architectural Design and Research Institute Co., Ltd., Urumqi 830047, China; nxjun163@163.com
* Correspondence: mingtaoliu0210@163.com (M.L.); macailong@xju.edu.cn (C.M.)

Abstract

Aggressive ions attack reinforcing steel in saline soil environments, and once the passive film on HRB400 steel destabilizes, localized corrosion spreads rapidly. Most studies vary the concentration of a single ion; how the SO_4^{2-}/Cl^- ratio governs film breakdown remains unclear. HRB400 specimens were immersed in simulated concrete pore solution and dosed stepwise with solid salts. Single-chloride and single-sulfate systems were used as controls; combined systems had SO_4^{2-}/Cl^- ratios of 1, 3 and 5. OCP, LPR and EIS were recorded at every step, with SEM/EDS on selected specimens. With chloride alone the passive film destabilized at 0.03–0.04 mol/L Cl^- (mean OCP); with sulfate alone the corrosion current density fell up to 0.05 mol/L SO_4^{2-}, and the destabilization occurred only at 0.11–0.12 mol/L. Raising the ratio shifted destabilization to 0.05–0.06, 0.06–0.07 and 0.11–0.12 mol/L, about 1.57, 1.86 and 3.29 times the chloride-only value, and at 0.10 mol/L Cl^- (240 h) mean icorr fell from 7.71 to 5.98, 3.19 and 1.26 μA/cm² (n = 3). Na^+ and K^+ were not varied independently; the concentrations refer to the pore solution. Sulfate therefore delays rather than prevents destabilization, and the ratio, not the chloride concentration alone, determines when the film fails.

Keywords: saline soil corrosion; durability; electrochemical impedance spectroscopy; sulfate-to-chloride concentration ratio; HRB400 reinforcing steel; passive film

Academic Editor: Xingwen Jia

Received: 31 October 2026
Revised: 19 November 2026
Accepted: 23 November 2026
Published: 25 November 2026

Copyright: © 2026 by the authors. Licensee MDPI, Basel, Switzerland. This article is an open access article distributed under the terms and conditions of the Creative Commons Attribution (CC BY) license.

1. Introduction

The durability failure of reinforced concrete structures arises mostly from corrosion of the reinforcement, and chloride attack is the main cause. In the alkaline interior of concrete (pH about 12.5–13.5), a passive film a few nanometers thick, with an FeOOH-enriched outer layer, forms spontaneously on the steel, and the corrosion current density is only 10^{-7} A/cm² [1]. As Cl^- migrates inward it accumulates on the steel surface, adsorbs onto and displaces the OH^- of the film and perforates it locally, after which pitting becomes autocatalytic [2]; the concentration at which the film is destabilized is the critical chloride concentration, a key input to transport calculation and life prediction [3]. The

corrosion products ($Fe(OH)_2$, $Fe(OH)_3$, FeOOH) occupy 2–6 times the volume of the original metal [4] and crack the cover, setting up the accelerated "corrosion–cracking–further corrosion" process.

Saline soils, chloride-contaminated groundwater and the zone of water-level fluctuation are often rich in both SO_4^{2-} and Cl^- [5], in proportions that vary with region, depth and season. SO_4^{2-} competes with Cl^- for adsorption sites on the film and can also enter it and alter its composition and semiconducting properties, so the destabilization condition in a combined medium is not fixed by the Cl^- concentration alone but depends on SO_4^{2-}/Cl^- concentration ratios.

The critical chloride concentration is the usual index of depassivation, but its value is not unique. Angst [3] found differences of nearly two orders of magnitude between reported values, arising mainly from the judgment criterion and the test medium rather than from the steel. In saturated $Ca(OH)_2$ at pH 13.5, general breakdown of carbon steel requires a chloride concentration of 1–2 mol/L, whereas pit initiation occurs one to two orders of magnitude lower, two different stages of destabilization in one system [6]; Peng [7] further showed that the critical value changes with the electrochemical criterion adopted. Without a unified criterion the effect of sulfate cannot be compared across studies.

Explanations center on competitive adsorption: SO_4^{2-} preferentially occupies the active sites and suppresses Cl^- adsorption, retarding depassivation [8–10]. This accounts for corrosion lying between the two single-ion systems, but not for the non-monotonic behavior—pitting of 321 stainless steel is progressively alleviated as SO_4^{2-}/Cl^- concentration ratios rise from 1 to 3 [11], whereas 304 stainless steel repassivates fastest at a ratio of 1:2 and more slowly away from it [12], which also implicates surface charge and the double layer. Sulfate is itself aggressive: it corrodes steel in chloride-free sulfoaluminate pore solution [13], and metastable pitting appears above about 0.014 mol/L SO_4^{2-} in alkaline sulfate solution [14]. Speciation matters too: reduced HS^- forms an Fe–S film that raises the critical concentration [15], and the Ca and Cr content of the film changes its resistance to depassivation [16,17].

Environmental conditions shift these regularities. Raising the film formation temperature from 20–40 to 50–60 °C lowers the critical concentration by about 15.8%, with sulfate protective only at low chloride concentration [18], while Na_2SO_4 and $MgSO_4$ affect the corrosion current in opposite directions over 27 months of concrete exposure [19]. pH acts independently: changing only the pH alters the film kinetics and structure of 2507 duplex steel in chloride-free solution [20], and for HRB400 a fall from pH 12.5 to 9.5 lowers the film resistance by one to two orders of magnitude, comparable with the effect of chloride [21]. Because pH and chloride concentration usually change together [22], the pH control must be stated, or an apparent sulfate effect may be a pH shift.

Electrochemistry gives the macroscopic response of the film; composition and structure require surface analysis, where combined ToF-SIMS and XPS separate adsorption from incorporation [23,24] and in situ Raman spectroelectrochemistry tracks corrosion products without removing the specimen [25]. Scale-up is a further question: thresholds from pore solution do not transfer directly to mortar [26], and at member scale EIS, the most widely used method, is affected by geometry and reinforcement layout, so impedance parameters are comparable only between similar members [27–29].

Life prediction follows the framework of chloride transport, critical concentration and corrosion-induced cracking, with probabilistic treatment of the scatter in critical concentration and diffusivity [30], oxygen diffusion differences in piles [31], a multi-field FEM-PD model for non-uniform corrosion under combined attack [32], EIS assessment of LC3 concrete [33] and temperature-dependent thresholds [34]. In all of them, the critical chloride concentration enters as a constant, sulfate enters as a diffusion acceleration term

or an apparent index, and the SO_4^{2-}/Cl^- concentration ratio is never an independent variable.

To address these gaps, tests were carried out in 500 mL of saturated $Ca(OH)_2$ solution containing 0.1 mol/L NaOH and 0.3 mol/L KOH (pH 13.62), with three parallel specimens in each group. Solid salts were added once every 24 h. In groups A, C, D and E, the chloride concentration rose by 0.01 mol/L per step, and in groups C, D and E, the sulfate concentration rose by 0.01, 0.03 and 0.05 mol/L per step, so that the SO_4^{2-}/Cl^- ratio was kept constant; group B received sulfate alone, at 0.01 mol/L per step. Every chloride-bearing system therefore reached a given chloride concentration after the same cumulative exposure, with 10 steps in groups A, C and D and 20 in groups B and E. Besides the two single-ion systems used as controls, three sulfate-rich mixed systems were tested. The onset of electrochemical destabilization is marked by a single operational endpoint: the first concentration step at which the open-circuit potential (OCP) falls below −380 mV (vs. SCE) and remains below it in all later steps. OCP and LPR were recorded at every step, and SEM/EDS was used to examine the morphology and elemental distribution before and after destabilization.

2. Materials and Methods

2.1. Materials

HRB400 hot-rolled ribbed steel bars (Xinjiang Bayi Iron & Steel Co., Ltd. (Baosteel Group), Urumqi, Xinjiang, China) with a nominal diameter of 12 mm were used to fabricate the working electrodes; their chemical composition is given in Table 1. The electrodes were encapsulated in Phoenix E44 bisphenol-A epoxy resin with a DETA (Nantong Xingchen Synthetic Material Co., Ltd., Nantong, Jiangsu, China) room-temperature curing agent, so that the specimen retains a fixed geometry and does not deform or dissolve during long immersion in the test solution. Anhydrous ethanol, anhydrous sodium sulfate (>99.9%), anhydrous sodium chloride, sodium hydroxide (>99.5%), potassium hydroxide (>99.5%) and calcium hydroxide (>99.5%) were of analytical grade (Sinopharm Chemical Reagent Co., Ltd., China) and were used as received.

Table 1. Chemical composition of the steel reinforcement (wt.%).

Steel Grade	Fe	C	Si	Mn	P	S
HRB400	97.89	0.22	0.53	1.31	0.026	0.027

The bars were cut into 10 mm long specimens, and one transverse cross-section served as the working surface. Each specimen was embedded in epoxy resin in a poly(vinyl chloride) mold; after curing, the working face was ground flat and its exposed area confined to 1.0 cm^2. This face was abraded with 400-, 800-, 1000- and 1500-grit paper and then polished to a mirror finish with 1.0 and 0.3 μm diamond pastes. The opposite face was connected to a copper wire with copper foil tape to provide the electrical contact, and all other faces were sealed with epoxy resin (Figure 1). Three parallel specimens were prepared for each group. Before use, the specimens were ultrasonically cleaned and stored sealed in a desiccator.

The simulated pore solution was prepared from distilled water as saturated $Ca(OH)_2$ containing 0.1 mol/L NaOH and 0.3 mol/L KOH, with a pH of about 13.6 [35]; the corrosion cell had an effective volume of 500 mL (Figure 2). Five aggressive solutions were used to reproduce the ionic composition of the saline soil: group A was a single-chloride solution, group B was a single-sulfate solution, and groups C–E were combined-salt solutions with $c(SO_4^{2-})/c(Cl^-)$ = 1, 3 and 5. Complete deterioration of the passive film required a

higher aggressive-ion concentration in the single-sulfate system (group B) and in the combined system of the highest ratio (group E), so the concentrations investigated were set to 0.20 mol/L SO_4^{2-} in group B and 0.20 mol/L Cl^- in group E, the latter corresponding to 1.0 mol/L SO_4^{2-}; these values served as a common upper test limit. The specimen numbering and the composition of the aggressive media are given in Table 2.

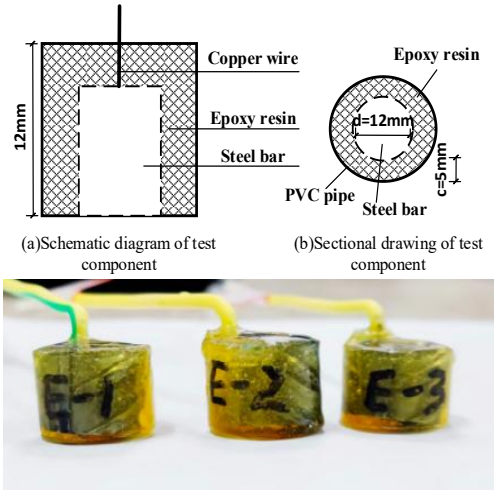


Figure 1. Dimensions and appearance of the specimen.

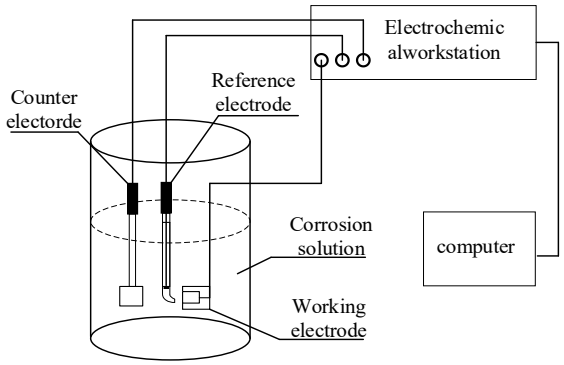


Figure 2. Schematic diagram of the corrosion cell.

Table 2. Specimen designations and design of aggressive medium concentrations.

Group	Sample No.	Number of Cycles	NaCl Added per Step (g)	Na_2SO_4 Added per Step (g)	$c(SO_4^{2-})/c(Cl^-)$
A	A-1,2,3	10	0.292	–	0
B	B-1,2,3	20	–	0.710	–
C	C-1,2,3	10	0.292	0.710	1
D	D-1,2,3	10	0.292	2.131	3
E	E-1,2,3	20	0.292	3.551	5

The three ratios were set from a survey of soils and groundwater in typical saline-soil regions of Xinjiang (Figure 3), carried out jointly with the Xinjiang Water Resources Survey and Design Institute. In both media the SO_4^{2-}/Cl^- molar ratio clusters around 1, with 0.7, 1.2 and 1.8 the most frequent values; it is systematically higher in soils than in groundwater and exceeds 10 in high-sulfate districts. A ratio of 1, at which the two ions are equimolar, therefore served as the reference, and ratios of 3 and 5 were chosen to cover the upper part of the distribution, that is, sulfate-dominant saline soils.

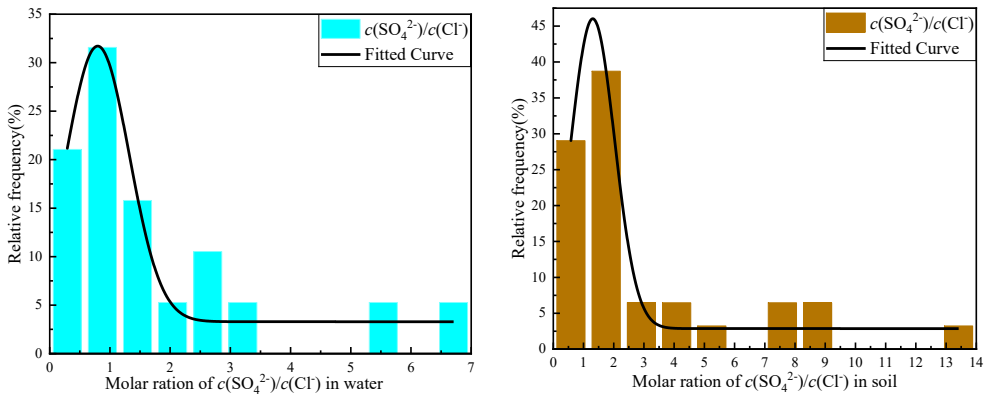


Figure 3. Relative frequency distribution of the SO_4^{2-}/Cl^- concentration ratio in (**a**) groundwater (n = 79); (**b**) soil (n = 43).

2.2. Test Methods

The encapsulated specimens were immersed in the simulated pore solution for passivation. Preliminary tests showed that the electrochemical parameters became essentially stable after the specimens had been kept sealed and static in this solution for 24 h. After 10 d of passivation, with the OCP varying by less than ±2 mV per 10 min, the passive film was considered to have formed and to be stable, and the deterioration tests were started immediately.

The tests were carried out by stepwise quantitative addition of solid salts in a corrosion cell of fixed effective volume of 500 mL. Every system started from 0.00 mol/L, and the concentration was raised in 0.01 mol/L steps, each step being held for 24 h; a given chloride concentration was therefore reached after the same number of steps, and hence after the same cumulative exposure, in all systems, so that the systems are compared at matched chloride concentration and matched cumulative exposure. The cell was opened only while the solid reagents were added and was otherwise sealed, to limit evaporation and CO_2 ingress. According to the dosing sequence and sulfate-to-chloride ratios of Table 2, analytical-grade NaCl and anhydrous Na_2SO_4 were weighed to 0.001 g and added, and the solution was stirred magnetically until clear. At selected cycles, a sample was taken to determine the actual concentrations of Cl^- and SO_4^{2-}; at the remaining steps, the nominal concentration calculated from Equation (1) was used. To keep the liquid volume unchanged, the aliquot withdrawn (about 5 mL) was replaced by an equal volume of stock solution of the same composition and pH (13.6). The specimen was then held at each concentration for 24 h before the electrochemical measurements. All tests were conducted at room temperature, 25 °C (±1 °C). The masses added in each step were calculated according to Equation (1):

$$m = \Delta c \cdot \mathrm{V} \cdot \mathrm{M} \quad (1)$$

where

m: the mass of solid salt to be weighed at that step (g);

Δ_c: the concentration increment of the target ion at that step (mol/L);

V: the solution volume of the corrosion cell (0.5 L);

M: the molar mass of the corresponding salt, taken as 58.44 g/mol for NaCl and 142.04 g/mol for Na_2SO_4.

The Cl^- was determined by an ion-selective electrode (JY-20 rapid chloride tester, Dalian Huade Instrument Co., Ltd., Dalian, Liaoning, China), SO_4^{2-} with a benchtop sulfate meter (LB-1805, Qingdao Lvbo Environmental Protection Equipment Co., Ltd., Qingdao, Shandong, China) and pH with a glass electrode (PHS-25, Shanghai Kuosi Electronic Co.,

Ltd. (APURE), Shanghai, China). Both electrodes were calibrated against standards prepared in the base pore solution of the same alkalinity (pH = 13.62) and comparable ionic strength, with four standards and the base solution as the zero point. The concentration measured with these instruments was taken as the effective concentration at each measurement point; the values in Table 2 are nominal dosing concentrations, whereas those measured at the selected cycles are listed in Table A6.

2.3. Electrochemical Measurements

Electrochemical measurements, including OCP, linear polarization resistance (LPR) and electrochemical impedance spectroscopy (EIS), were carried out on an RST6210F electrochemical workstation (Zhengzhou Shiruisi Instrument Technology Co., Ltd., Zhengzhou, Henan, China) in a standard three-electrode cell, with the HRB400 specimen as the working electrode, a saturated calomel electrode (SCE, saturated KCl salt bridge) as the reference and a 20 mm × 20 mm platinum sheet as the counter electrode. Once the OCP had stabilized to within ±2 mV per 10 min, EIS was recorded first and LPR second; the LPR test was started only after the OCP had returned to a steady state, so that the DC polarization would not disturb an interface that had not yet recovered its equilibrium.

For EIS, a sinusoidal perturbation of 10 mV amplitude was applied over 0.1 Hz–100 kHz; the instrument saturates below 0.1 Hz, which was therefore adopted as the lower limit. The phase angle at 0.1 Hz remains between 30° and 80° in all five systems , so the low-frequency plateau of the spectra was not reached and the fitted R_1 and Rct describe the response within the measured window: R_1 + Rct is a lower bound on the low-frequency resistance rather than a direct-current value.

In the LPR test, the potential was scanned over OCP ± 10 mV at 10 mV/min, and the polarization resistance was taken from the slope of the linear i–E relation, $Rp = \Delta E/\Delta i$. The corrosion current density was then calculated as $i_{corr} = B/Rp$ (Equation (2)), with B = 26 mV for all corrosion-stage data (from the 0.01 mol/L step after the first salt addition) and B = 52 mV for the passive-stage data of Figures 4 and 5; because the two stages are converted with different B, they are not compared numerically through i_{corr}. The i_{corr} values reported here are therefore estimates conditional on this choice of B; because the same B is applied within each stage, they are compared in relative terms and not as absolute corrosion rates.

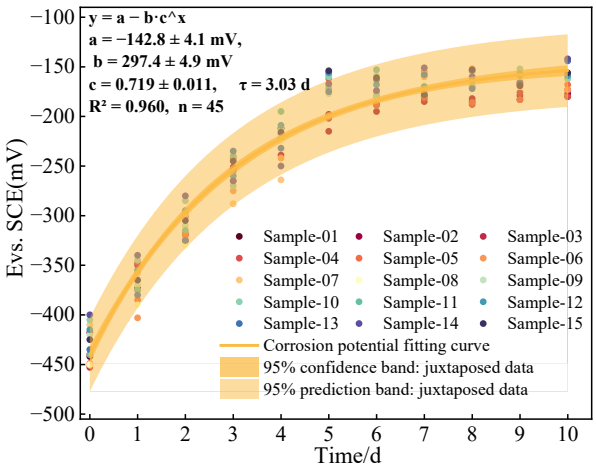


Figure 4. Fitted of the OCP curves of the steel during the passivation stage.

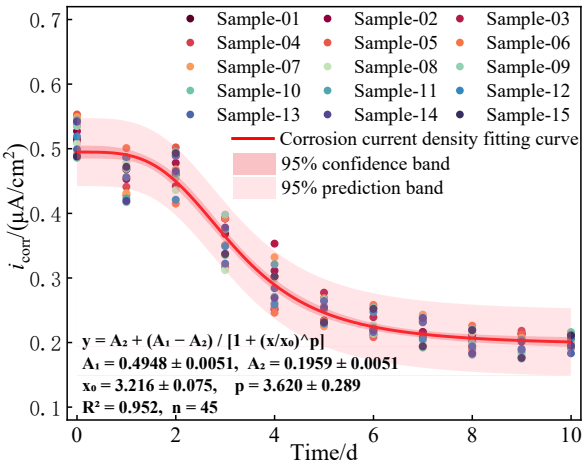


Figure 5. Fitted curves of the i_{corr} evolution of the specimens during the passivation stage (i_{corr} computed with B = 52 mV).

2.4. Morphology and Composition Characterization

The micromorphology of the corrosion products was observed with an FEI Quanta 400 HV scanning electron microscope (SEM, Thermo Fisher Scientific (FEI Company), Hillsboro, OR, USA) operated at an accelerating voltage of 20 kV and a working distance of 10 mm. The elemental composition of the products was analyzed with the attached EDAX energy-dispersive X-ray spectrometer (EDS, EDAX Inc., Mahwah, NJ, USA) at an accelerating voltage of 20 kV, an X-ray take-off angle of 35° and an acquisition live time of 60 s. Before SEM observation the specimen surface was sputter-coated with carbon to improve its electrical conductivity. After removal from the solution the specimens were dehydrated with anhydrous ethanol and dried at room temperature before observation, so that the original appearance of the surface corrosion products was preserved.

3. Results

3.1. Passive Film and Corrosion Severity Criteria

In an alkaline environment, the passive film on the steel surface usually has a bilayer structure, with a dense spinel-type Fe_3O_4 inner layer and a loose $FeOOH/Fe_2O_3$ outer layer [36], and its integrity can be assessed indirectly from electrochemical parameters such as the OCP and icorr. Previous studies show that the steel is in the passive stage when the OCP is above −380 mV (vs. SCE) [35,37]. For icorr, Andrade and Alonso [38] established a classification of corrosion severity from laboratory and field data that has been adopted by RILEM TC 154-EMC [39]: below 0.1 μA/cm² the state is negligible (passive), 0.1–0.5 μA/cm² is low corrosion, 0.5–1 μA/cm² moderate, and above 1 μA/cm² high, at which the steel can be regarded as already corroding. That classification is scaled by the annual corrosion depth and serves to grade the condition of a structure, not to fix the moment at which the passive film loses stability. The two indicators therefore serve different purposes and cannot replace each other: icorr and Rp describe the rate of dissolution at the interface, whereas the OCP describes the state of the interface. They do not always change at the same concentration. Localized attack raises the anodic current before the mixed potential has shifted appreciably, so the largest step in icorr usually occurs at or before the step at which the OCP crosses—by one step in the chloride-bearing systems and by four to five steps in the sulfate-only system (Tables A2 and A8). The potential crossing therefore marks a later stage of the transition, and in the chloride-bearing systems a more definitive one. In this work the operational endpoint defined in Section 1 marks the onset of passive-film destabilization, whereas icorr describes only the degree of the transition. The same absolute threshold was applied to all five systems, because the base electrolyte, the

steel grade and the passivation procedure were identical and only the amount and the type of the added aggressive ions differed.

Figure 4 presents the evolution of OCP of the 15 steel specimens over 10 d of passivation, together with the corresponding fits obtained with a three-parameter asymptotic exponential model (R^2 = 0.960). The initial OCP (d0) was −450 mV (vs. SCE); it shifted progressively towards more positive values as passivation proceeded and leveled off after day 6, fluctuating slightly around −180 mV. This indicates that the passive film had essentially formed but had not yet attained a fully passive state. In Figure 5, icorr was fitted with a four-parameter logistic function (R^2 = 0.952), and icorr was about 0.20 μA/cm² after day 6. To ensure that the passive film remained stably adherent, the specimens were removed after 10 d of immersion.

The polarization resistance is taken directly from the LPR measurement, and the corrosion current density follows from it:

$$i_{\text{corr}} = \frac{i}{\Delta E}\left\{\frac{\beta_a \beta_c}{2.303(\beta_a a + \beta_c c)}\right\} = \frac{B}{R_{\text{p}}} \quad (2)$$

$$B = \frac{\beta_a \beta_c}{2.303(\beta_a + \beta_c)} \quad (3)$$

where

R_P: the polarization resistance, defined as ΔE/(Δi·A), where A is the working area of the electrode (1.0 cm², Section 2.1); R_P is therefore an area-normalized resistance in Ω·cm².

β_a and β_c: the slopes of the anodic and cathodic polarization curves, respectively.

B: the Stern–Geary constant, equal to 52 mV for steel in the passive state and 26 mV in the active corrosion state [18]. In this work B = 52 mV was used for the passivation stage and B = 26 mV for the whole corrosion stage; with R_P in kΩ·cm² and B in mV, i_{corr} obtained from Equation (2) is directly in μA/cm².

Figure 6 presents the Nyquist plots (a) and Bode plots (b) of the steel at different treatment times. In Nyquist plots, a larger diameter of the capacitive arc generally indicates better corrosion resistance [40]. The figure shows a representative spectrum from one of the three parallel tests, and all three replicate tests exhibited good reproducibility. As shown in Figure 6a, the radius of the capacitive loop was relatively small in the initial state (d0); it increased continuously from d1 to d5, reflecting the continuous growth of the passive film, while the growth amplitude decreased markedly from d6 to d10 and the curves gradually coincided, indicating that the passive film tended to stabilize. In the Bode plots (Figure 6b), the maximum phase angle increased with passivation time and stabilized at approximately 70° from day 6 onward, displaying pronounced capacitive characteristics; this indicates that the passive film became increasingly complete and that the interface possessed a strong charge-blocking capability. Taken together, the OCP, LPR, and EIS results all tended to stabilize, demonstrating that a relatively complete passive film had formed on the working electrode surface, upon which the subsequent degradation tests could be carried out.

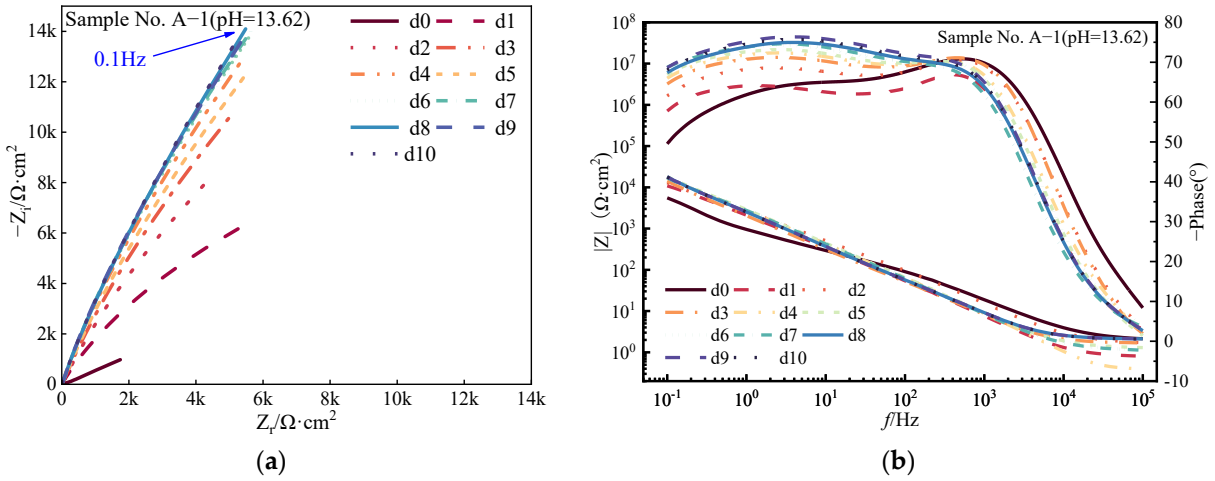


Figure 6. EIS data of the specimens during the passivation stage: (**a**) Nyquist plot evolution. (**b**) Bode plot evolution.

3.2. Effect of Single Chloride Attack

The OCP reflects the thermodynamic state of the interface, whereas icorr reflects the corrosion rate [3]; the two therefore have independent sources of error [8,41]. Here the onset of electrochemical destabilization is defined by a single operational endpoint: the first concentration step at which the OCP falls below −380 mV (vs. SCE), a level at which the corrosion probability of steel exceeds 91.4% [35]. The endpoint is registered only if the OCP remains below this level in all later steps, with readings taken at the end of each 24 h step. icorr is obtained from the Rp measured by LPR through the Stern–Geary relation with B = 26 mV, and is used only to describe the degree of corrosion and its relative change, not to locate the endpoint. The endpoint is operational rather than thermodynamic: it does not by itself demonstrate that the film has broken down.

As shown in Figure 7, at Cl^- concentrations not exceeding 0.02 mol/L the OCP of the three specimens remained in the passive region, i_{corr} was 0.16–0.27 μA/cm² and R_p was 96.3–162.5 kΩ·cm² (Figure 8; detailed values of R_p and i_{corr} as a function of chloride concentration are given in Table A1). At 0.03 mol/L the OCP of every specimen fell below −380 mV and the specimens entered the corrosion state, while i_{corr} was only 0.26–0.33 μA/cm² and R_p 78.8–100.0 kΩ·cm², still within the low-corrosion range. The three specimens did not cross at exactly the same step: specimen A-1 reached −397 mV at 0.03 mol/L, whereas A-2 and A-3 reached −388 and −385 mV only at 0.04 mol/L, which is why the interval is reported as 0.03–0.04 mol/L. Only at 0.04 mol/L did i_{corr} jump to 1.17–2.53 μA/cm², up to 15.8 times for individual specimens, with R_p falling to 10.3–22.2 kΩ·cm². Thereafter the OCP stabilized between −584 and −634 mV, i_{corr} stabilized at 4.6–8.1 μA/cm² (24–42 times the initial value), and R_p fell to 3.3–5.8 kΩ·cm², 96–98% lower than the initial value. The critical destabilization concentration of the single-chloride system can therefore be determined as 0.03–0.04 mol/L. Its width is set by the 0.01 mol/L step of the dosing protocol together with the one-step spread between replicate specimens, and is therefore not a measure of the uncertainty of the reported values.

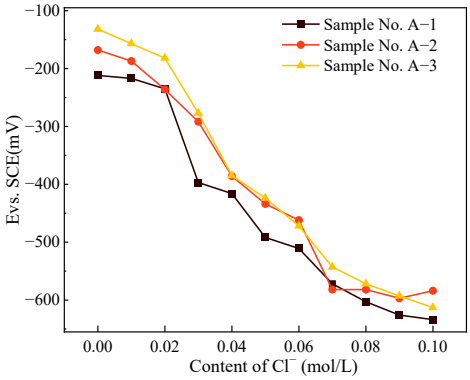


Figure 7. Evolution of the OCP of the steel with chloride concentration.

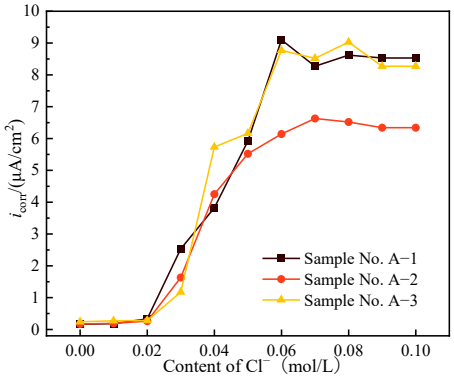


Figure 8. Evolution of the i_{corr} of the steel with chloride concentration.

The evolution of the impedance spectra is consistent with the above trend (Figure 9). Taking specimen A-1 as an example, in the early stage of deterioration the radius of curvature of the capacitive arc in the Nyquist plot (Figure 9a) was large and the maximum phase angle in the Bode plot was stable at about 70°, so that the interface was dominated by capacitive blocking; as the Cl^- concentration increased, the capacitive arc contracted progressively and the phase angle decreased continuously; and at 0.05 mol/L the radius of the capacitive arc in the Nyquist plot shrank sharply and the maximum phase angle in the Bode plot (Figure 9b) dropped to about 45°, after which the arc radius hardly changed any further, with the passive film on the steel surface having largely lost its blocking ability.

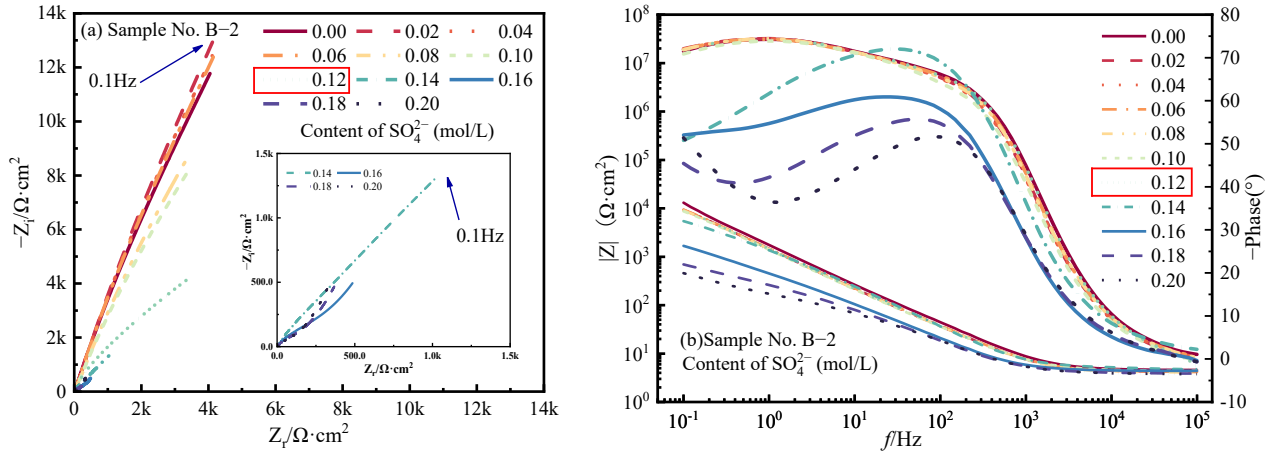


Figure 9. EIS of the steel specimens in the chloride-only simulated pore solution at different chloride concentrations: (**a**) Nyquist plots. (**b**) Bode plots. (The red box in the legend marks the concentration step at which the OCP falls below −380 mV (vs. SCE)).

https://doi.org/10.3390/ma19235002

3.3. Effect of Single Sulfate Attack

In the single-sulfate system the OCP exhibits a distinct two-stage character (Figure 10). At SO_4^{2-} concentrations of 0.05 mol/L and below, no continuous negative shift in the OCP was observed; i_{corr} decreased from a mean of 0.12 μA/cm² to 0.06–0.07 μA/cm², 44–50% lower than the initial value (Figure 11), corresponding to an increase in R_p from 173.3–288.9 kΩ·cm² to 236.4–866.7 kΩ·cm² (Table A2). Once the concentration exceeded 0.05 mol/L the OCP began to shift slowly in the negative direction, and it did not fall below −380 mV until the concentration reached 0.11–0.12 mol/L; thereafter the negative shift accelerated and stabilized between −427 and −445 mV. Electrochemical weakening nevertheless preceded this crossing: the mean R_p had already fallen to 106.6 kΩ·cm² at 0.06 mol/L, and at 0.07 mol/L all three specimens exceeded 1 μA·cm⁻². For all specimens i_{corr} had already reached the high-corrosion grade at SO_4^{2-} concentrations of 0.07–0.08 mol/L and stabilized at 3.60–3.63 μA/cm² at 0.20 mol/L. The two indicators therefore separate by four to five dosing steps in this system.

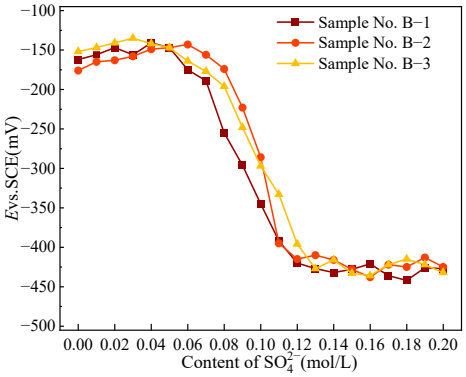


Figure 10. Evolution of OCP with sulfate content.

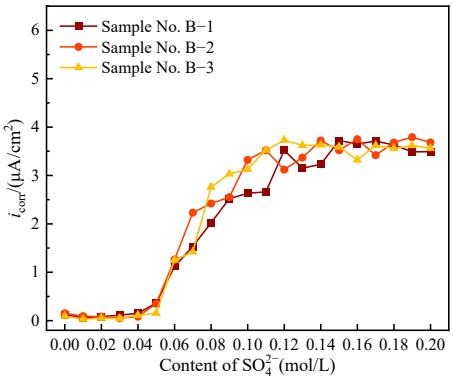


Figure 11. Evolution of i_{corr} with sulfate content.

In the early stage of deterioration the radius of the capacitive arc in the Nyquist plots (Figure 12a) of specimen B-2 was always maintained at a relatively high level and even increased slightly; in the Bode plots (Figure 12b) the maximum phase angle remained at 65–70° and began to decrease slowly only after the SO_4^{2-} concentration in the solution exceeded 0.06 mol/L, contracting sharply only at 0.12 mol/L.

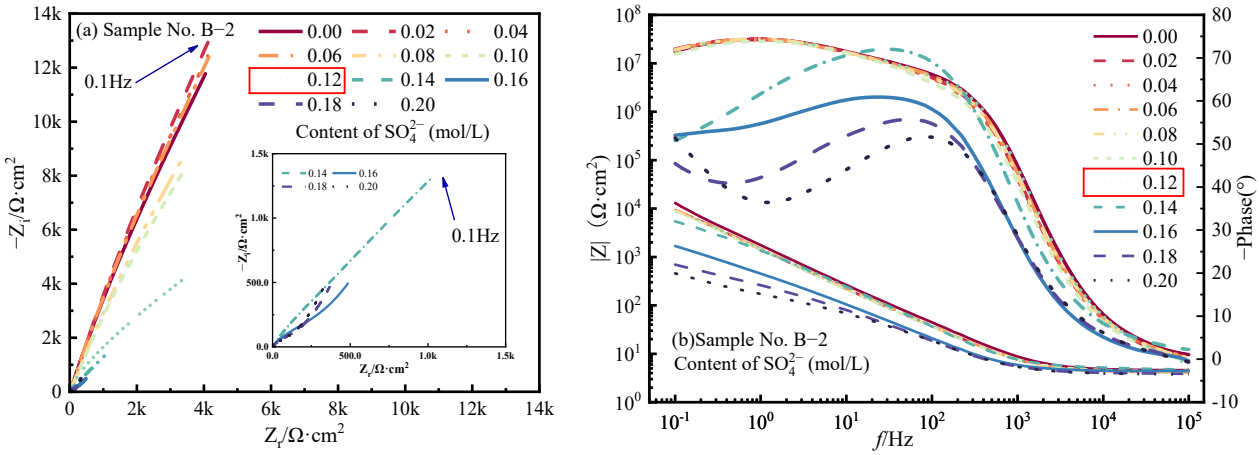


Figure 12. EIS of the steel specimens in the sulfate-only simulated pore solution at different sulfate concentrations: (**a**) Nyquist plots; (**b**) Bode plots.

3.4. Combined Chloride–Sulfate Solutions with Different Concentration Ratios

Figure 13 and Tables A3–A5 show the chloride concentration at which the passive film of each system loses stability. Taking the mean OCP of the three specimens, this concentration moves to a higher value as the ratio rises: 0.05–0.06 mol/L in group C, 0.06–0.07 mol/L in group D and 0.11–0.12 mol/L in group E, against 0.03–0.04 mol/L in the chloride-only system. Figure 14 and Tables A3–A5 show how icorr evolves. In groups C and D it jumps at 0.06 and 0.07 mol/L to 1.61 and 1.28 μA/cm², and then continues to rise; in group E it rises gradually instead and reaches only 1.26 μA/cm² at 0.10 mol/L. The two indicators are not synchronous: icorr reaches the high-corrosion grade at the same step as the OCP in groups C and D, one to two steps earlier in group E and four to five steps earlier in the sulfate-only system. At 0.10 mol/L, the concentration all systems reached after the same cumulative exposure of 240 h, the mean icorr falls from 7.71 to 5.98, 3.19 and 1.26 μA/cm² as the ratio rises; only E-1 had lost stability by then, E-2 and E-3 doing so between 0.11 and 0.12 mol/L (Table A8). Counted from each system's own destabilization step, the mean icorr one step later is 4.60 ± 1.00 μA/cm² in the chloride-only system and 3.33 ± 1.38, 2.35 ± 0.18 and 2.89 ± 0.37 μA/cm² at ratios of 1, 3 and 5, so every sulfate-bearing system remains below the chloride-only system, and the two higher ratios differ by less than the scatter between parallel specimens.

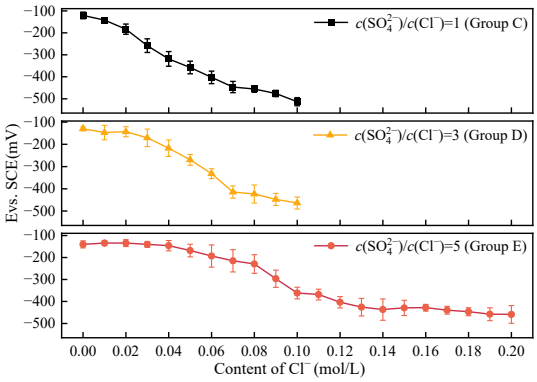


Figure 13. Evolution of OCP of the specimens at $c(SO_4^{2-}):c(Cl^-)$ = 1, 3 and 5.

The three specimens of a group do not lose stability at exactly the same step (open circles in Figure 15): A-1 falls below −380 mV at 0.02–0.03 mol/L and A-2 and A-3 at 0.03–0.04 mol/L; C-2 at 0.04–0.05 mol/L and C-1 and C-3 at 0.05–0.06 mol/L; all three specimens of group D at 0.06–0.07 mol/L; and in group E, E-1 at 0.09–0.10 mol/L and E-2 and E-3 at

0.11–0.12 mol/L (Table A8). Expressed as midpoints of these mean-OCP crossing intervals, the concentration required is about 1.57, 1.86 and 3.29 times that of the chloride-only system.

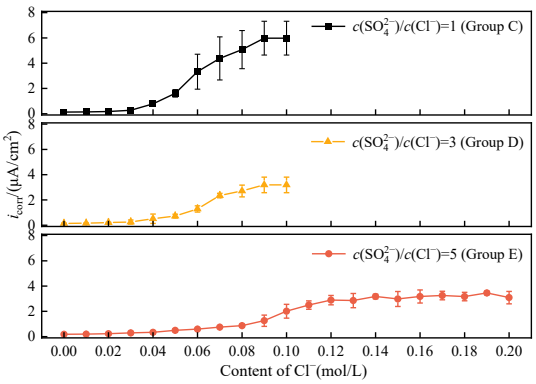


Figure 14. Evolution of i_{corr} of the specimens at $c(SO_4^{2-})$:$c(Cl^-)$ = 1, 3 and 5.

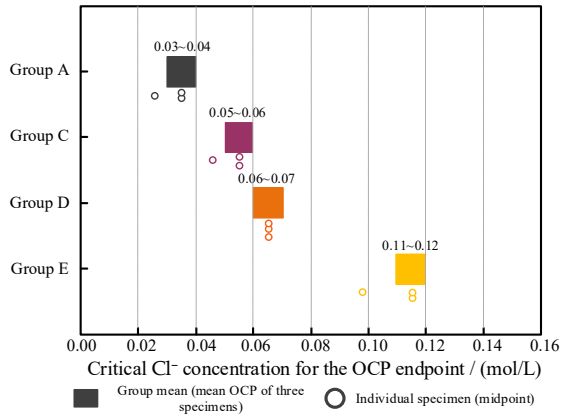


Figure 15. Ranges of Cl^- concentration over which the OCP endpoint is reached in each system.

Figures 16–18 present the impedance responses of specimens C-3, D-3 and E-2 to the increasing concentration of aggressive ions. In the combined solution with a ratio of 1, the capacitive arc in the Nyquist plot of group C (Figure 16a) contracted markedly as soon as the Cl^- concentration reached 0.06 mol/L, and the maximum phase angle in the Bode plot (Figure 16b) dropped from about 70° to near 40°; for group D in the combined solution with a ratio of 3, the capacitive arc in the Nyquist plot (Figure 17a) decreased only slowly and the phase angle fluctuated slightly in the Cl^- concentration range of 0.04–0.05 mol/L, and it contracted significantly only around 0.07 mol/L; for group E in the combined solution with a ratio of 5, the radius of the capacitive arc in the Nyquist plot (Figure 18a) was always maintained at a relatively high level while the Cl^- concentration was below 0.10 mol/L, began to contract once the Cl^- concentration exceeded 0.10 mol/L, and even after contraction the arc radius remained larger than that of the other groups at the same stage. Correspondingly, the phase curves in the Bode plots change from the single-peak form of group C (Figure 16b), through the peak splitting of group D (Figure 17b), into the double-peak feature of group E (Figure 18b), which first decreases and then increases.

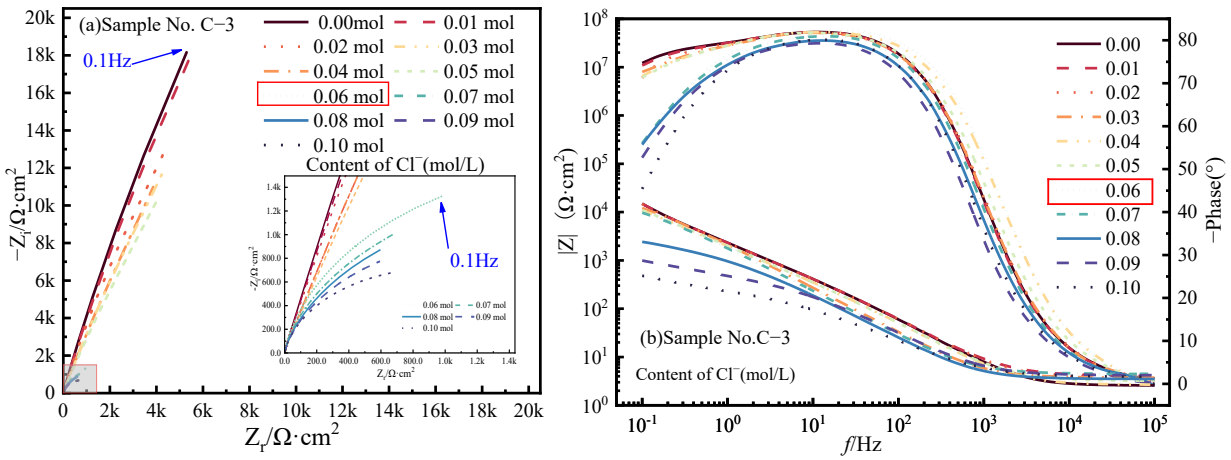


Figure 16. EIS of the steel specimens at different chloride concentrations ($c(SO_4^{2-})$:$c(Cl^-)$= 1): (**a**) Nyquist plots. (**b**) Bode plots.

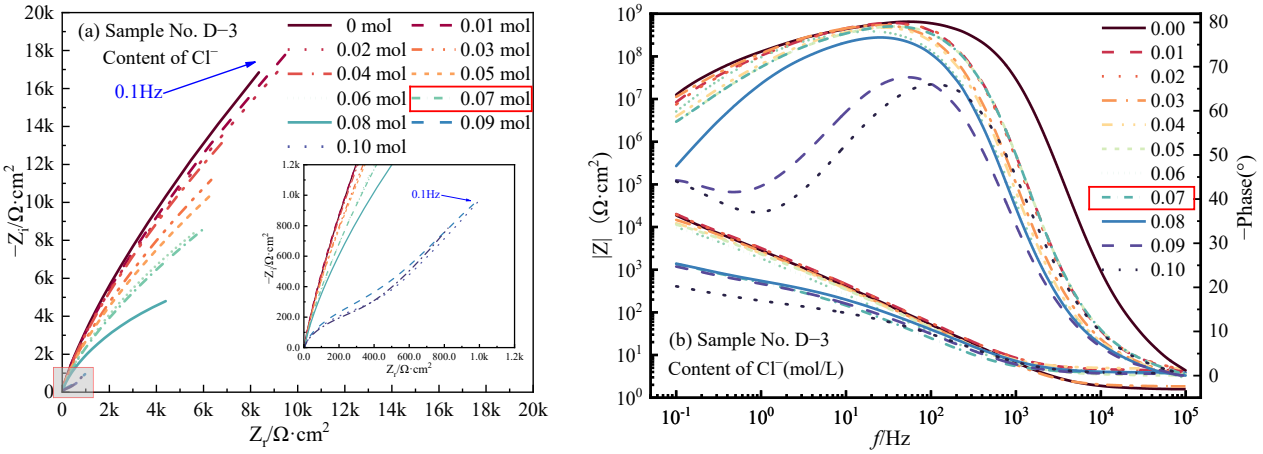


Figure 17. EIS of the steel specimens at different chloride concentrations ($c(SO_4^{2-})$:$c(Cl^-)$= 3): (**a**) Nyquist plots. (**b**) Bode plots.

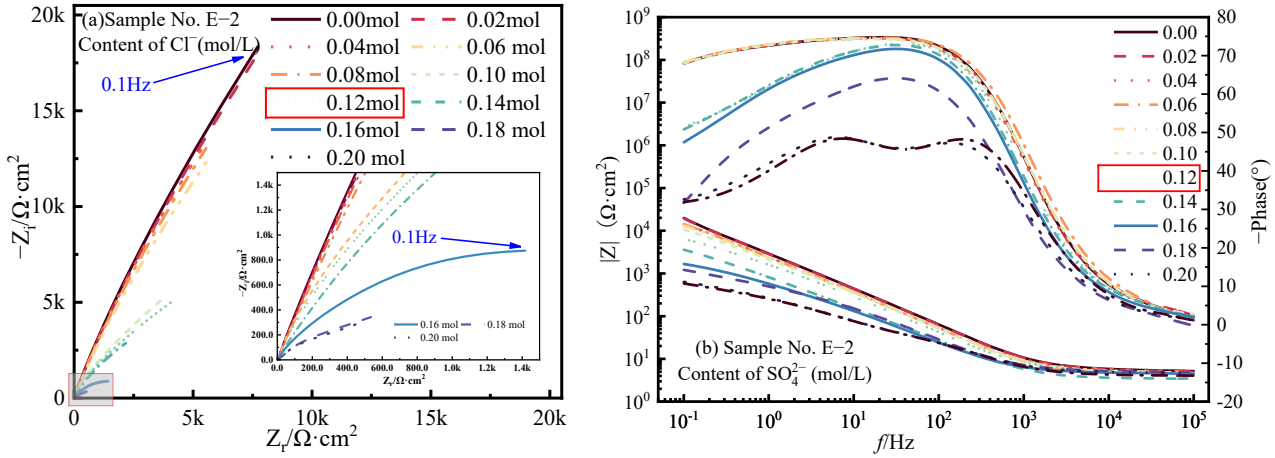


Figure 18. EIS of the steel specimens at different chloride concentrations ($c(SO_4^{2-})$:$c(Cl^-)$= 5): (**a**) Nyquist plots. (**b**) Bode plots.

3.5. Equivalent Circuit Fitting

For the EIS response of coating-like specimens in aggressive media, a two-time-constant model is usually adopted [41]. As shown in Figure 19, the equivalent circuit used in this work is R(Q(R(QR))); the spectra were fitted with ZSimpWin V3.60 (EChem Software,

Ann Arbor, MI, USA) by complex non-linear least squares with modulus weighting ($|Z|^{-1}$), and χ^2 is the weighted sum of squared residuals normalized by the degrees of freedom. The fitting results are listed in Table 3, where the χ^2 values of all groups lie between 9.56×10^{-5} and 9.86×10^{-4}; this shows that the residuals are small in absolute terms but does not establish that the two time constants are independently resolved, and the model is therefore used as a descriptive parameterization of the measured spectra. The passive film is not an ideally polarizable interface, so the constant phase elements CPE1 and CPE2 are used instead of ideal capacitors. Their exponents n1 and n2 reflect the degree of deviation from ideal capacitive behavior caused by surface heterogeneity and roughness, while the amplitude parameters Y0,1 and Y0,2 are proportional to the capacitance of the passive film and of the electric double layer, respectively. One spectrum per group is fitted in Table 3; the three parallel specimens of each group were all measured, and their polarization resistance is reported with its spread in Tables A1–A5 (maximum-to-minimum ratios up to 4), so the fitted parameters are used only for between-group comparisons at the same chloride concentration.

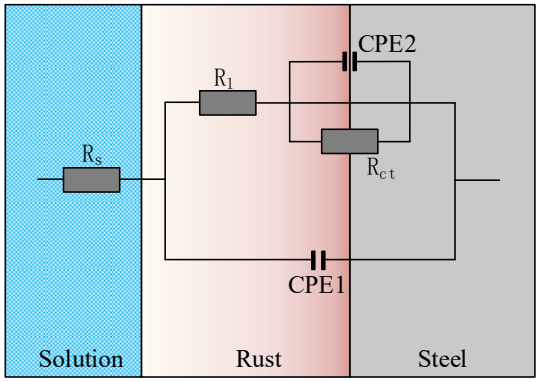


Figure 19. Equivalent circuit diagram for the corrosion stage.(The background colors are schematic only and are used to distinguish the solution, the rust layer and the steel substrate; the interfaces are not sharp at the microscopic scale).

In the single-chloride system, the fitted R_1 falls from 4.49×10^3 to 2.11×10^2 Ω·cm² between 0.01 and 0.06 mol/L Cl^- (a decrease of 95%), while the fitted R_{ct} falls from 2.48×10^4 to 3.21×10^3 Ω·cm² over the same range (87%) and to 1.91×10^3 Ω·cm² at 0.08 mol/L (92%; Table 3). The decrease is not gradual. R1 stays between 3.68×10^3 and 4.49×10^3 Ω·cm² up to 0.02 mol/L, drops to 1.13×10^3 Ω·cm² at 0.03 and to 6.99×10^2 Ω·cm² at 0.04 mol/L, and then remains within 2.1–2.7 × 10^2 Ω·cm² from 0.06 mol/L onwards. Rct falls sharply between 0.01 and 0.02 mol/L ($2.48 \times 10^4 \rightarrow 4.81 \times 10^3$ Ω·cm²), varies between 3.6×10^3 and 5.6×10^3 Ω·cm² up to 0.05 mol/L, and settles at 1.6–1.9 × 10^3 Ω·cm² beyond 0.07 mol/L. The largest drop in R_1 therefore coincides with the OCP crossing (0.03–0.04 mol/L), whereas that in R_{ct} occurs earlier (0.01–0.02 mol/L); after the crossing, both quantities remain low.

In the combined-salt systems (groups C, D and E), both fitted resistances increase with the concentration ratio at a given Cl^- concentration (Table 3). At 0.04 mol/L, R1 is 1.23 × 10^3, 3.02×10^3 and 5.05×10^3 Ω·cm² for groups C, D and E, i.e., 1.8, 4.3 and 7.2 times those of group A, while Rct is 1.61×10^4, 3.92×10^4 and 1.34×10^5 Ω·cm², i.e., 4.5, 11.0 and 37.5 times in the fitted values. These factors describe how the model distributes the impedance between the two time constants; they are not separately measured film and charge-transfer resistances.

Table 3. Equivalent circuit fitting results of the corrosion EIS data in different aggressive environments.

	Content (mol/L)	Rs (Ω·cm²)	CPE1, Y0,1 (S·sᵃ·cm⁻²)	CPE1, n1 [0 < n < 1]	R_1 (Ω·cm²)	CPE2, Y0,2 (S·sᵃ cm⁻²)	CPE2, n2 [0 < n < 1]	R_{ct} (Ω·cm²)	χ^2
A-1	0.01	3.08	9.343×10^{-5}	0.8572	4486	3.711×10^{-5}	0.7087	24,805	1.746×10^{-4}
	0.02	5.73	8.287×10^{-5}	0.8638	3681	3.748×10^{-5}	0.6835	4808	1.944×10^{-4}
	0.03	5.55	8.676×10^{-5}	0.8676	1134	3.645×10^{-5}	0.6765	5601	1.678×10^{-4}
	0.04	6.20	9.387×10^{-5}	0.8543	699	3.42×10^{-5}	0.672	3568	1.635×10^{-4}
	0.05	6.12	8.802×10^{-5}	0.8591	562	4.044×10^{-5}	0.6361	5011	1.381×10^{-4}
	0.06	5.25	1.592×10^{-4}	0.8381	211	2.671×10^{-4}	0.4537	3213	3.828×10^{-4}
	0.07	3.69	1.635×10^{-4}	0.8261	214	2.983×10^{-4}	0.4071	1561	4.398×10^{-4}
	0.08	1.85	9.443×10^{-5}	0.8185	268	3.305×10^{-4}	0.5247	1908	5.917×10^{-4}
	0.09	2.00	3.401×10^{-4}	0.8257	233	1.338×10^{-4}	0.8412	1920	3.196×10^{-4}
	0.10	3.57	2.222×10^{-4}	0.8167	253	6.645×10^{-4}	0.5219	1614	2.168×10^{-4}
B-2	0.01	6.29	1.16×10^{-4}	0.8451	5246	3.491×10^{-4}	0.8049	153,501	1.735×10^{-4}
	0.02	5.63	1.414×10^{-4}	0.8156	5004	3.634×10^{-4}	0.8352	167,102	1.098×10^{-4}
	0.04	3.34	1.486×10^{-4}	0.8148	7337	1.597×10^{-4}	0.701	158,110	1.504×10^{-4}
	0.06	4.47	1.489×10^{-4}	0.8131	7813	1.421×10^{-4}	0.8267	95,850	9.857×10^{-4}
	0.08	4.14	1.548×10^{-4}	0.8115	6221	1.031×10^{-4}	0.8155	25,303	7.424×10^{-4}
	0.10	4.26	1.550×10^{-4}	0.8113	5159	6.689×10^{-4}	0.8038	6711	6.904×10^{-4}
	0.12	5.10	1.526×10^{-4}	0.8106	3679	5.477×10^{-4}	0.7337	7111	7.385×10^{-4}
	0.14	4.31	3.915×10^{-4}	0.0386	1821	5.637×10^{-4}	0.5078	7257	8.201×10^{-4}
	0.16	4.93	1.112×10^{-4}	0.8607	1460	3.695×10^{-4}	0.4607	8210	4.906×10^{-4}
	0.18	4.4	9.672×10^{-4}	0.9157	1543	4.778×10^{-4}	0.5282	7131	1.163×10^{-4}
	0.20	3.85	3.818×10^{-4}	0.7826	1463	1.703×10^{-3}	0.4844	7177	4.228×10^{-4}
C-3	0.01	2.36	7.028×10^{-5}	0.8892	5108	6.993×10^{-5}	0.6948	25,500	2.615×10^{-4}
	0.02	4.16	6.134×10^{-5}	0.8975	4434	6.569×10^{-5}	0.7021	25,800	2.882×10^{-4}
	0.03	3.64	6.216×10^{-5}	0.8956	2765	6.616×10^{-5}	0.6983	23,850	2.691×10^{-4}
	0.04	2.81	6.285×10^{-5}	0.8956	1227	7.109×10^{-5}	0.6536	16,101	2.710×10^{-4}
	0.05	3.00	6.393×10^{-5}	0.8937	1204	6.95×10^{-5}	0.6561	12,050	1.991×10^{-4}
	0.06	4.12	9.214×10^{-5}	0.9143	897	1.448×10^{-4}	0.4928	12,290	3.220×10^{-4}
	0.07	4.56	1.012×10^{-4}	0.9049	540	1.093×10^{-4}	0.5228	8010	3.091×10^{-4}
	0.08	3.54	1.254×10^{-4}	0.8972	984	6.072×10^{-4}	0.3856	5183	2.353×10^{-4}
	0.09	4.21	1.222×10^{-4}	0.8660	310	1.53×10^{-3}	0.4286	7727	1.419×10^{-4}
	0.10	3.86	3.244×10^{-4}	0.7773	207	3.387×10^{-3}	0.5604	5510	9.558×10^{-5}
D-3	0.01	4.46	5.641×10^{-5}	0.9208	4752	3.855×10^{-5}	0.5866	76,100	2.701×10^{-4}
	0.02	4.54	5.740×10^{-5}	0.9199	4388	3.987×10^{-5}	0.5777	73,300	2.695×10^{-4}
	0.03	4.79	5.926×10^{-5}	0.9158	4503	4.499×10^{-5}	0.5164	50,071	2.110×10^{-4}
	0.04	4.88	6.242×10^{-5}	0.9168	3019	6.342×10^{-5}	0.4877	39,214	2.231×10^{-4}
	0.05	4.34	6.117×10^{-5}	0.9148	3321	5.72×10^{-5}	0.5040	22,489	2.256×10^{-4}
	0.06	3.39	6.348×10^{-5}	0.9170	2256	6.888×10^{-5}	0.4718	8529	2.254×10^{-4}
	0.07	3.76	1.642×10^{-4}	0.8623	779	9.794×10^{-4}	0.5401	7072	1.836×10^{-4}
D-3	0.08	3.83	1.050×10^{-4}	0.8557	354	9.883×10^{-4}	0.5418	7573	3.925×10^{-4}
	0.09	3.57	1.314×10^{-4}	0.8589	290	1.147×10^{-3}	0.5194	8129	4.017×10^{-4}
	0.10	3.66	1.518×10^{-4}	0.8253	102	3.569×10^{-3}	0.5000	6460	5.085×10^{-4}
E-2	0.01	4.96	7.948×10^{-5}	0.7864	5240	1.06×10^{-5}	0.8731	168,600	4.056×10^{-4}
	0.02	4.85	8.144×10^{-5}	0.7877	6283	1.024×10^{-5}	0.8726	164,000	3.876×10^{-4}
	0.04	5.08	7.786×10^{-5}	0.8607	5048	2.584×10^{-5}	0.5280	133,931	3.303×10^{-4}
	0.06	4.97	7.339×10^{-5}	0.8677	2766	3.668×10^{-5}	0.5354	74,410	4.015×10^{-4}
	0.08	4.86	7.161×10^{-5}	0.8762	1782	6.444×10^{-5}	0.5265	35,430	4.115×10^{-4}
	0.10	4.94	8.645×10^{-5}	0.8678	1744	1.367×10^{-4}	0.4759	32,208	6.627×10^{-4}
	0.12	5.11	9.621×10^{-5}	0.8614	1902	1.426×10^{-4}	0.4615	27,241	6.788×10^{-4}

0.14	3.46	1.356×10^{-4}	0.8618	939	2.143×10^{-4}	0.5802	22,560	1.530×10^{-4}
0.16	4.58	2.222×10^{-4}	0.8213	358	4.119×10^{-4}	0.5152	3358	1.708×10^{-4}
0.18	4.75	1.270×10^{-4}	0.8631	239	1.167×10^{-3}	0.5424	1350	8.456×10^{-4}
0.20	4.09	1.066×10^{-4}	0.8773	204	1.236×10^{-3}	0.5360	1176	9.198×10^{-4}

To avoid an excessively long table, the data of groups B and E are listed at intervals.

3.6. Microscopic Analysis

The passivated specimen was an extra parallel specimen removed after 10 d of immersion in the alkaline solution. The remaining specimens were sampled once the whole concentration series of their group had been completed and the electrochemical parameters had stabilized, and were taken out at the end of the last concentration step (0.10 mol/L Cl^- for group A, 0.20 mol/L SO_4^{2-} for group B, and 0.10, 0.10 and 0.20 mol/L Cl^- for groups C, D and E, respectively). The five specimens—A-1, B-2, C-3, D-3 and E-2—are those used for the impedance and polarization measurements, so that the electrochemical and microscopic observations refer to the same specimens. Because the number of dosing steps and the final concentration differ among the groups, the exposure time and the absolute ion concentration at sampling also differ (Table A7); the comparison of surface morphology between groups is therefore qualitative. Morphology was examined by scanning electron microscopy, and the elemental composition and maps were obtained by energy-dispersive spectroscopy (Figure 20).

After passivation (Figure 20a) the surface was completely covered by a dense, uniform layer of needle-like and flower-like crystals, closely packed in overlapping clusters, with no cracks, spalling or pits visible. In the elemental maps (Figure 20b), Fe and O appear as alternating bands along the machining direction, corresponding to the steel substrate and the oxygen-bearing surface layer, respectively, while S and Cl appear only as a faint, uniform background, without local enrichment.

After breakdown the morphology differed markedly between systems. In group A, the originally complete needle-like layer spalled over a wide area (Figure 20c), and the Fe signal covered almost the whole field of view (Figure 20d), leaving large areas of the steel exposed. In group B, by contrast, no bare substrate was exposed: the surface was covered by rough granular products (Figure 20e), the Fe map showed dark, low-signal regions, and S was enriched in discrete aggregates (Figure 20f).

As the sulfate proportion increases, the deposit on group C (Figure 20g) covers about one third of the field of view, markedly more than in group A; there, S and Cl occupy separate regions, and the sulfur-bearing area hardly overlaps the area where Cl is enriched (Figure 20h). On groups D and E, accumulations with undulating relief appear (Figure 20i,k), the dark, low-signal regions of the Fe map expand and the S-enriched aggregates grow accordingly and tend towards continuity (Figure 20j,l), while Cl still forms a continuous, branching distribution in group D and contracts into scattered small dots in group E.

Sulfate therefore does not eliminate the damaging effect of chloride. The maps show a sulfur-bearing region that becomes more continuous as its proportion rises, but every specimen examined here was taken out after its whole concentration series had been completed, so the maps give the final state of each group and cannot show the order in which deposition and depassivation occurred. Whether this region is a nanoscale adsorbed sulfate layer or a precipitated sulfur-bearing solid phase, whether chloride penetrates it, and whether the film fails exactly where it is absent—none of these can be answered from elemental maps acquired at 20 kV. The retarding effect of the sulfur-rich region is therefore proposed only as a hypothesis consistent with the electrochemical response, and awaits verification by depth profiling and valence-state analysis.

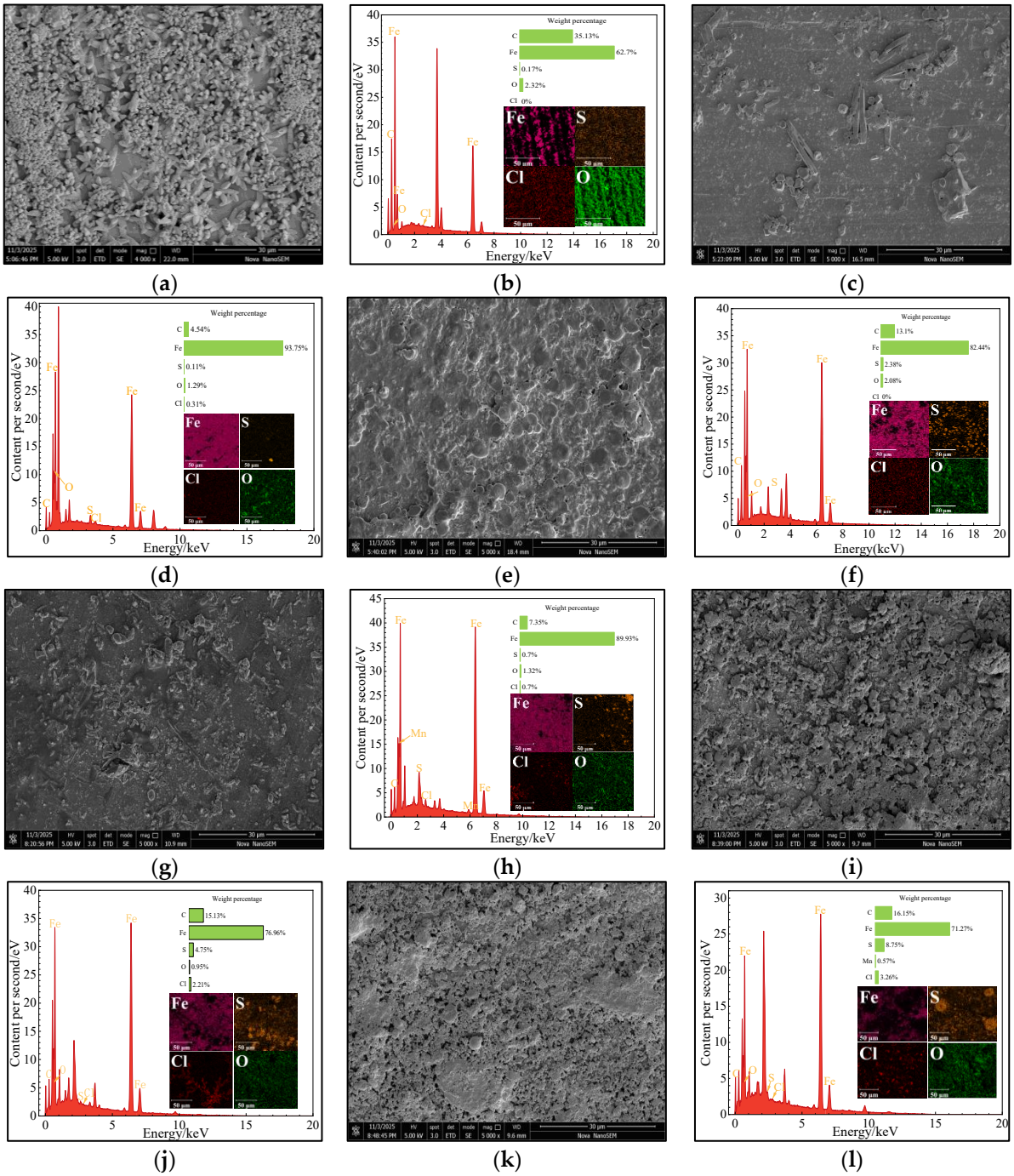


Figure 20. SEM images (**a**,**c**,**e**,**g**,**i**,**k**) and the corresponding EDS spectra and elemental maps (**b**,**d**,**f**,**h**,**j**,**l**) of the steel surface: (**a**,**b**) after passivation; (**c**,**d**) after breakdown of the passive film in the single-chloride system; (**e**,**f**) in the single-sulfate system; (**g**,**h**), (**i**,**j**) and (**k**,**l**) at $c(SO_4^{2-})$:$c(Cl^-)$ = 1, 3 and 5, respectively.

4. Discussion

4.1. Difference Between the Simulated Pore Solution System and Real Concrete

All tests were carried out on HRB400 specimens immersed directly in a simulated pore solution, to which chloride and sulfate were added stepwise as solid salts; no mortar or concrete cover was present. This isolates the steel–solution interface, so that the ion ratio is fixed by design and the surface state and the electrochemical response can be followed continuously. In a member, chloride must first cross the cover, where part of it is bound by C–S–H and by the AFm phase as Friedel's salt [42,43], so the concentration that

reaches the steel is lower than that at the exposed surface and rises more slowly. Porosity, saturation and drying–wetting cycles govern the transport rate, and carbonation lowers the pH of the outer pore solution and alters its binding capacity. None of these processes is represented here: the data describe the steel–solution interface, not the steel behind a cover.

The stepwise protocol compresses the whole concentration sequence into a few weeks, with each step held for 24 h, whereas in service the same change in concentration may take months or years, during which deposits grow, transform and rearrange. The endpoint therefore answers whether the film can be maintained at a given concentration, not how long it can be maintained. Temperature was held at 25 ± 1 °C and did not vary; its effects on dissolved oxygen, and on the solubility of the reaction products are consequently outside the scope of this work.

Sodium sulfate raises the sulfate concentration, and it necessarily adds sodium ions and raises the ionic strength; the stepwise addition also shifts the pH slightly, by an amount that differs between systems. These variables change in the same direction as the ratio and cannot be separated from it in the present design, so the conclusions apply to the ratio along the salt-addition path used here.

4.2. Effect of the Sulfate-to-Chloride Concentration Ratio on the Destabilization Threshold

The concentration at which this endpoint is reached rises with the ratio: 0.03–0.04 mol/L Cl^- in the chloride-only system and 0.05–0.06, 0.06–0.07 and 0.11–0.12 mol/L at ratios of 1, 3 and 5 (mean OCP; every specimen crosses within one step of its group interval), which is about 1.57, 1.86 and 3.29 times the chloride-only value on an interval-midpoint basis. The sulfate-only system behaves differently: sulfate does not accelerate damage up to 0.05 mol/L and keeps the anodic current below its initial value, but beyond that concentration the kinetic indicators (R_p and i_{corr}) turn well before the potential. The mean Rp falls from 390–530 kΩ·cm² to 106.6 kΩ·cm² at 0.06 mol/L and icorr exceeds the high-corrosion grade at 0.07–0.08 mol/L, while the OCP endpoint is reached only at 0.11–0.12 mol/L. The two indicators therefore separate by four to five dosing steps in this system, and the potential crossing should not be read as the onset of kinetic deterioration.

4.3. Competitive Adsorption and the Concentration Window of Sulfate Protection

Competitive adsorption is the explanation most often invoked for the retarding effect of sulfate, and we adopt it here as a hypothesis rather than as an established finding. Sulfate and chloride compete for the same sites on the oxide surface, so adsorbed sulfate occupies sites at which chloride would otherwise initiate dissolution, raising the chloride concentration required for breakdown [12,44,45]. The same mechanism also bounds the effect: at high concentrations sulfate is itself aggressive, forming gypsum and ettringite [46,47], so the delay does not increase indefinitely with the sulfate content and the corrosion current rises again above a certain concentration. In the EDS maps the sulfur-rich region becomes more continuous as the ratio rises, but EDS at 20 kV cannot distinguish a nanometer-thick adsorbed layer from a solid phase [48], and the maps show only the end of each sequence; which of the two is at work—adsorption, a solid deposit, or both—and whether it delayed the onset of localized corrosion therefore remains undetermined. Answering that question requires TOF-SIMS depth profiling and XPS, which could not be carried out in this work and are the subject of our continuing study.

4.4. Implications for Durability Assessment and Engineering Practice

This endpoint is an interface-scale quantity. Its purpose is to provide a comparable measure of film destabilization for a given pore solution and a given steel grade; it does not replace the chloride limits used in the structural design of concrete. By raising the ion

concentration at the steel surface in steps with 24 h of exposure at each step and taking the OCP endpoint as the criterion, the chloride concentration at which the passive film destabilizes in a given system can be established within a few weeks, at a cost far below that of long-term exposure tests; the method can therefore be used to compare how different steel grades, surface treatments or inhibitors affect corrosion resistance.

For existing structures, the most directly transferable conclusion of this work concerns sampling and interpretation rather than a numerical value. First, sulfate—or the sulfate-to-chloride ratio—should be determined together with the chloride content: at the same chloride content the film can be at different stages of stability, so the chloride content alone is not a sufficient index. Second, the sampling positions must correspond, that is, have the same depth and the same exposed surface; otherwise the comparison loses its meaning. Third, the priority for monitoring alarms: the OCP is the quantity most easily obtained on site, and half-cell potential measurement is well established, but the present results show that in the single-sulfate system the kinetic indicators precede the OCP endpoint by four to five dosing steps, whereas in the chloride-bearing systems they are essentially synchronous with it. Using potential as the only warning therefore comes late in sulfate-dominated environments; corrosion-rate parameters should raise the alarm first, with potential used to confirm the trend.

5. Conclusions

The behavior of the passive film on HRB400 steel in a saturated $Ca(OH)_2$ simulated concrete pore solution was followed during stepwise addition of chloride and sulfate, with the SO_4^{2-}/Cl^- concentration ratio set to 1, 3 and 5. The following conclusions can be drawn:

1. In the chloride-only system the interface destabilized between 0.03 and 0.04 mol/L Cl^-, and the transition is abrupt: i_{corr} rises by a factor of about six within one concentration step, and the polarization resistance falls accordingly.
2. Sulfate alone is not aggressive over a wide range. Up to 0.05 mol/L SO_4^{2-} both kinetic indicators moved in the protective direction, and the OCP endpoint was reached only at 0.11–0.12 mol/L; the two indicators respond four to five dosing steps apart.
3. Raising the SO_4^{2-}/Cl^- ratio means that more chloride is required before the passive film loses stability: the mean-OCP crossing interval rises from 0.03–0.04 mol/L in the chloride-only system to 0.05–0.06, 0.06–0.07 and 0.11–0.12 mol/L at ratios of 1, 3 and 5, about 1.57, 1.86 and 3.29 times that of the chloride-only system.
4. Sulfate also lowers the corrosion rate once the film has destabilized: at matched nominal chloride concentration and exposure time (0.10 mol/L, 240 h), the mean icorr falls from 7.71 to 5.98, 3.19 and 1.26 μA/cm² as the SO_4^{2-}/Cl^- ratio rises from 1 to 3 and 5, and one step after its own endpoint every sulfate-bearing system also remains below the chloride-only system.
5. Sulfate postpones destabilization rather than preventing it: with sulfate alone the kinetic indicators improve up to 0.05 mol/L SO_4^{2-} and the OCP endpoint is reached only at 0.11–0.12 mol/L, and in the mixed systems the critical chloride concentration rises with the ratio. The postponement holds within a limited concentration window—once it is passed the corrosion current rises again—and within the pore-solution compositions tested.

Author Contributions: Conceptualization, M.L. and C.M.; methodology, M.L. and Y.Y.; software, M.L.; validation, M.L. and Y.Y.; formal analysis, M.L.; investigation, M.L. and Y.Y.; resources, C.M. and X.N.; data curation, M.L.; writing—original draft preparation, M.L.; writing—review and edit-

ing, M.L., Y.Y., C.M. and X.N.; visualization, M.L.; supervision, C.M. and X.N.; project administration, C.M. and X.N.; funding acquisition, C.M. and X.N. All authors have read and agreed to the published version of the manuscript.

Funding: This research was funded by the National Natural Science Foundation of China (grant numbers 52478215 and 52438010) and by the Xinjiang Uygur Autonomous Region Tianshan Talent Program for Young Top-Notch Talents (grant number 2023TSYCCX0110).

Data Availability Statement: The original contributions presented in the study are included in the article. Further inquiries can be directed to the corresponding authors.

Acknowledgments: The authors thank Lina Zhou and her student Yijie Chen for their guidance on the electrochemical measurements and data analysis, and the School of Civil Engineering and Architecture, Xinjiang University, for providing the experimental site, instruments and equipment. The authors also thank the research group for helpful discussions on the experimental design and on the revision of the manuscript. During the preparation of this manuscript, the authors used DeepSeek Harness (DeepSeek-V4.1-Flash, 2026) only for language polishing and improvement of expression.

Conflicts of Interest: Authors Xiangjun Niu was employed by Xinjiang Architectural Design and Research Institute Co., Ltd., Urumqi 830047, China. The remaining authors declare that the research was conducted in the absence of any commercial or financial.

Appendix A

Table A1. Evolution of i_{corr} and R_p of the specimens in group A during the corrosion stage.

Time/d	Content of Cl^- (mol/L)	i_{corr} (μA/cm²)					R_p (kΩ·cm²)			
		A-1	A-2	A-3	Mean	SD	A-1	A-2	A-3	Mean
1	0.01	0.16	0.17	0.24	0.19	0.04	162.50	152.94	108.33	141.26
2	0.02	0.18	0.19	0.27	0.21	0.05	144.44	136.84	96.30	125.86
3	0.03	0.33	0.26	0.28	0.29	0.04	78.79	100.00	92.20	90.55
4	0.04	2.53	1.63	1.17	1.78	0.69	10.28	15.95	22.22	16.15
5	0.05	3.82	4.25	5.73	4.60	1.00	6.81	6.12	4.54	5.82
6	0.06	5.92	5.52	6.16	5.87	0.32	4.39	4.71	4.22	4.44
7	0.07	9.10	6.14	8.77	8.00	1.62	2.86	4.23	2.96	3.35
8	0.08	8.27	6.63	8.52	7.81	1.03	3.14	3.92	3.05	3.37
9	0.09	8.62	6.52	9.03	8.06	1.35	3.02	3.99	2.88	3.30
10	0.10	8.53	6.34	8.27	7.71	1.20	3.05	4.10	3.14	3.43

Tables A1–A5, i_{corr} = B/Rp with B = 26 mV.

Table A2. Evolution of i_{corr} and R_p of the specimens in group B during the corrosion stage.

Time/d	Content of SO_4^{2-} (mol/L)	i_{corr} (μA/cm²)					R_p (kΩ·cm²)			
		B-1	B-2	B-3	Mean	SD	B-1	B-2	B-3	Mean
1	0.01	0.12	0.15	0.09	0.12	0.03	216.67	173.33	288.89	226.30
2	0.02	0.06	0.09	0.03	0.06	0.03	433.33	288.89	866.67	529.63
3	0.03	0.08	0.08	0.05	0.07	0.02	325.00	325.00	520.00	390.00
4	0.04	0.11	0.05	0.04	0.06	0.04	236.36	520.00	650.00	468.79
5	0.05	0.15	0.08	0.11	0.11	0.03	173.33	325.00	236.36	244.90
6	0.06	0.36	0.35	0.15	0.29	0.12	72.22	74.29	173.33	106.61
7	0.07	1.12	1.26	1.25	1.21	0.08	23.21	20.63	20.80	21.55
8	0.08	1.53	2.23	1.42	1.73	0.44	16.99	11.66	18.31	15.65
9	0.09	2.02	2.42	2.76	2.40	0.37	12.87	10.74	9.42	11.01
10	0.10	2.52	2.55	3.03	2.70	0.29	10.32	10.19	8.58	9.70

11	0.11	2.63	3.32	3.13	3.03	0.36	9.89	7.83	8.31	8.68
12	0.12	2.66	3.52	3.52	3.23	0.50	9.77	7.38	7.38	8.18
13	0.13	3.52	3.12	3.73	3.46	0.31	7.39	8.33	6.97	7.56
14	0.14	3.15	3.37	3.62	3.38	0.24	8.25	7.72	7.18	7.72
15	0.15	3.23	3.72	3.63	3.53	0.26	8.05	6.99	7.16	7.40
16	0.16	3.72	3.52	3.59	3.61	0.10	6.99	7.38	7.24	7.20
17	0.17	3.65	3.75	3.32	3.57	0.23	7.12	6.93	7.83	7.29
18	0.18	3.71	3.42	3.62	3.58	0.15	7.01	7.60	7.18	7.26
19	0.19	3.63	3.68	3.56	3.62	0.06	7.16	7.06	7.30	7.17
20	0.20	3.49	3.79	3.62	3.63	0.15	7.45	6.86	7.18	7.16

Table A3. Evolution of i_{corr} and R_p of the specimens in group C during the corrosion stage.

Time/d	Content of Cl^- (mol/L)	i_{corr} (μA/cm²)					R_p (kΩ·cm²)			
		C-1	C-2	C-3	Mean	SD	C-1	C-2	C-3	Mean
1	0.01	0.11	0.14	0.13	0.13	0.02	236.36	185.71	200.00	207.36
2	0.02	0.13	0.15	0.14	0.14	0.01	200.00	173.33	185.71	186.35
3	0.03	0.17	0.17	0.18	0.17	0.01	152.94	152.94	144.44	150.11
4	0.04	0.35	0.22	0.24	0.27	0.07	74.28	118.18	108.33	100.26
5	0.05	0.93	0.56	0.84	0.78	0.19	27.96	46.43	30.95	35.11
6	0.06	1.54	1.94	1.36	1.61	0.30	16.88	13.40	19.12	16.47
7	0.07	3.38	4.68	1.92	3.33	1.38	7.69	5.56	13.54	8.93
8	0.08	4.96	5.72	2.46	4.38	1.71	5.242	4.55	10.56	6.78
9	0.09	5.64	6.22	3.36	5.07	1.51	4.61	4.18	7.74	5.51
10	0.10	6.86	6.64	4.44	5.98	1.34	3.79	3.92	5.86	4.52

Table A4. Evolution of i_{corr} and R_p of the specimens in group D during the corrosion stage.

Time/d	Content of Cl^- (mol/L)	i_{corr} (μA/cm²)					R_p (kΩ·cm²)			
		D-1	D-2	D-3	Mean	SD	D-1	D-2	D-3	Mean
1	0.01	0.13	0.11	0.18	0.14	0.04	200.00	236.36	144.44	193.60
2	0.02	0.17	0.15	0.14	0.15	0.02	152.94	173.33	185.71	170.66
3	0.03	0.22	0.23	0.17	0.21	0.03	118.18	113.04	152.94	128.05
4	0.04	0.11	0.43	0.22	0.25	0.16	236.36	60.47	118.18	138.34
5	0.05	0.23	0.37	0.93	0.51	0.37	113.04	70.27	27.96	70.42
6	0.06	0.57	0.72	0.87	0.72	0.15	45.61	36.11	29.88	37.20
7	0.07	1.02	1.51	1.32	1.28	0.25	25.49	17.22	19.70	20.80
8	0.08	2.51	2.16	2.37	2.35	0.18	10.36	12.04	10.97	11.12
9	0.09	2.74	2.23	3.16	2.71	0.47	9.49	11.66	8.228	9.79
10	0.10	3.73	2.52	3.32	3.19	0.62	6.97	10.32	7.83	8.37

Table A5. Evolution of i_{corr} and R_p of the specimens in group E during the corrosion stage.

Time/d	Content of Cl^- (mol/L)	i_{corr} (μA/cm²)					R_p (kΩ·cm²)			
		E-1	E-2	E-3	Mean	SD	E-1	E-2	E-3	Mean
1	0.01	0.22	0.17	0.15	0.18	0.04	118.18	152.94	173.33	148.15
2	0.02	0.24	0.27	0.07	0.19	0.11	108.33	96.29	371.42	192.01
3	0.03	0.33	0.22	0.13	0.23	0.10	78.79	118.18	200.00	132.32
4	0.04	0.39	0.33	0.15	0.29	0.12	66.67	78.79	173.33	106.26
5	0.05	0.46	0.36	0.18	0.33	0.14	56.52	72.22	144.44	91.06
6	0.06	0.63	0.42	0.42	0.49	0.12	41.27	61.90	61.90	55.02
7	0.07	0.66	0.53	0.57	0.59	0.07	39.39	49.06	45.61	44.69
8	0.08	0.78	0.72	0.74	0.75	0.03	33.33	36.11	35.13	34.86
9	0.09	0.97	0.73	0.88	0.86	0.12	26.80	35.62	29.54	30.65

10	0.10	1.72	0.83	1.23	1.26	0.45	15.12	31.32	21.13	22.52
11	0.11	2.62	1.56	1.85	2.01	0.55	9.92	16.67	14.05	13.55
12	0.12	2.73	2.64	2.12	2.50	0.33	9.52	9.85	12.26	10.54
13	0.13	3.26	2.88	2.52	2.89	0.37	7.97	9.03	10.31	9.10
14	0.14	3.38	2.92	2.26	2.85	0.56	7.69	8.90	11.504	9.36
15	0.15	3.23	3.32	2.97	3.17	0.18	8.05	7.83	8.75	8.21
16	0.16	3.16	3.46	2.32	2.98	0.59	8.23	7.51	11.21	8.98
17	0.17	3.22	3.67	2.64	3.18	0.52	8.07	7.08	9.85	8.33
18	0.18	3.36	3.52	2.87	3.25	0.34	7.74	7.39	9.06	8.06
19	0.19	3.12	3.53	2.86	3.17	0.34	8.33	7.36	9.09	8.26
20	0.20	3.32	3.42	3.45	3.40	0.07	7.83	7.60	10.32	8.58

Table A6. Nominal and measured concentrations of chloride and sulfate, and pH of the test solutions at selected cycles.

Group	Cycle	Cl^- Nominal (mol/L)	Cl^- Measured (mol/L)	SO_4^{2-} Nominal (mol/L)	SO_4^{2-} Measured (mol/L)	pH
A	2	0.02	0.020	0.00	0.001	13.61
	6	0.06	0.061	0.00	0.001	13.47
	10	0.10	0.098	0.00	0.001	13.34
B	2	0.00	0.000	0.02	0.021	13.52
	6	0.00	0.000	0.06	0.063	13.48
	10	0.00	0.000	0.10	0.102	13.48
	14	0.00	0.001	0.14	0.144	13.51
	20	0.00	0.001	0.20	0.207	13.48
C	2	0.02	0.022	0.02	0.022	13.62
	6	0.06	0.063	0.06	0.061	13.54
	10	0.10	0.097	0.10	0.100	13.50
D	2	0.02	0.020	0.06	0.053	13.62
	6	0.06	0.059	0.18	0.177	13.62
	10	0.10	0.107	0.30	0.304	13.61
E	2	0.02	0.021	0.10	0.103	13.62
	6	0.06	0.058	0.30	0.305	13.50
	10	0.10	0.102	0.50	0.506	13.47
	14	0.14	0.140	0.70	0.703	13.47
	20	0.20	0.207	1.00	1.004	13.47

Table A7. Exposure time and measured ion concentrations at the time of sampling.

Group	$c(SO_4^{2-})/c(Cl^-)$	Specimen	Sampling Stage	$C(Cl^-)$ (mol/L)	$C(SO_4^{2-})$ (mol/L)	Exposure (d)
A	Cl^- only	A-1	final step	0.10	0.00	10
B	SO_4^{2-} only	B-2		0.00	0.20	20
C	1	C-3		0.10	0.10	10
D	3	D-3		0.10	0.30	10
E	5	E-2		0.20	1.00	20

Table A8. Concentration steps at which each specimen crosses −380 mV and at which its icorr rises most steeply.

Group	Specimen	OCP Crossing Step (mol/L)	Largest Step in i_{corr} (mol/L)	Step Factor
A	A-1	0.02–0.03	0.03–0.04	7.7
	A-2	0.03–0.04	0.03–0.04	6.3

	A-3	0.03–0.04	0.04–0.05	4.9
B	B-1	0.10–0.11	0.06–0.07	3.1
	B-2	0.10–0.11	0.05–0.06	4.4
	B-3	0.11–0.12	0.06–0.07	8.3
C	C-1	0.05–0.06	0.04–0.05	2.7
	C-2	0.04–0.05	0.05–0.06	3.5
	C-3	0.05–0.06	0.04–0.05	3.5
D	D-1	0.06–0.07	0.05–0.06	2.5
	D-2	0.06–0.07	0.06–0.07	2.1
	D-3	0.06–0.07	0.04–0.05	4.2
E	E-1	0.09–0.10	0.09–0.10	1.8
	E-2	0.11–0.12	0.10–0.11	1.9
	E-3	0.11–0.12	0.05–0.06	2.3

References

1. Ghods, P.; Isgor, O.B.; Bensebaa, F.; Kingston, D. Angle-resolved XPS study of carbon steel passivity and chloride-induced depassivation in simulated concrete pore solution. *Corros. Sci*. **2012**, *58*, 159–167. https://doi.org/10.1016/j.corsci.2012.01.019.
2. Saremi, M.; Mahallati, E. A study on chloride-induced depassivation of mild steel in simulated concrete pore solution. *Cem. Concr. Res*. **2002**, *32*, 1915–1921. https://doi.org/10.1016/S0008-8846(02)00895-5.
3. Angst, U.; Elsener, B.; Larsen, C.K.; Vennesland, Ø. Critical chloride content in reinforced concrete—A review. *Cem. Concr. Res*. **2009**, *39*, 1122–1138. https://doi.org/10.1016/j.cemconres.2009.08.006.
4. Zhao, Y.X.; Ren, H.Y.; Dai, H.; Jin, W. Composition and expansion coefficient of rust based on X-ray diffraction and thermal analysis. *Corros. Sci*. **2011**, *53*, 1646–1658. https://doi.org/10.1016/j.corsci.2011.01.007.
5. Song, Y.; Wang, Y.; Wang, Y.; Liu, B. Chloride-induced rebar corrosion behavior in concrete within and above water level fluctuating zone under sulfate attack. *Constr. Build. Mater*. **2025**, *458*, 139640. https://doi.org/10.1016/j.conbuildmat.2024.139640.
6. Qiu, J.; Zhu, Y.; Xu, Y.; Li, Y.; Mao, F.; Wu, A.; Macdonald, D.D. Effect of chloride on the pitting corrosion of carbon steel in alkaline solutions. *J. Electrochem. Soc.* **2022**, *169*, 031501. https://doi.org/10.1149/1945-7111/ac580c.
7. Peng, Y.; Lin, Y.; Xia, R.; Dai, Z.; Zhang, W.; Liu, W. Electrochemical investigation of chloride ion-induced breakdown of passive film on P110 casing steel surface in simulated pore solution: Behavior and critical value determination. *Metals* **2024**, *14*, 93. https://doi.org/10.3390/met14010093.
8. Liu, C.; Mao, F.; Wang, J.; Li, B. Combined effect of chloride and sulfate ions on the corrosion behavior of Q355B steel in simulated concrete pore solution. *Mater. Today Commun*. **2024**, *40*, 109703. https://doi.org/10.1016/j.mtcomm.2024.109703.
9. Gong, K.; Liu, C.; Yang, M.; Mao, F. Effect of Cl^-, SO_4^{2-}, and pH on the corrosion behavior and depassivation mechanism of Q355B steel in simulated concrete pore solution. *J. Mater. Sci*. **2025**, *60*, 3518–3538. https://doi.org/10.1007/s10853-025-10668-1.
10. Li, J.; Liu, G.; Yu, W.; Liu, Z.; Zhang, Z.; Zhang, Y. Effects of chloride and sulfate ions on the corrosion of steel reinforcement in simulated concrete pore solution. *Acta Mater. Compos. Sin*. **2025**, *42*, 2775–2787. (In Chinese) https://doi.org/10.13801/j.cnki.fhclxb.20240719.003.
11. Shcherbakov, A.I.; Kasatkina, I.V.; Kasatkin, V.E.; Korosteleva, I.G.; Dorofeeva, V.N.; Kornienko, L.P. Influence of the stainless steel 321 (X18H10) structure on pitting corrosion in low-mineralized water. Inhibiting effect of sulfate and hydrocarbonate ions. *Int. J. Corros. Scale Inhib*. **2021**, *10*, 176–185. https://doi.org/10.17675/2305-6894-2021-10-1-10.
12. Pesqueira, C.M.; Luiz, L.A.; de Andrade, J.; Garcia, C.M.; Portella, K.F. The effect of chloride, sulfate, and ammonium ions on the semiconducting behavior and corrosion resistance of AISI 304 stainless steel passive film. *Matéria* **2023**, *28*, e20230139. https://doi.org/10.1590/1517-7076-rmat-2023-0139.
13. Morozov, Y.; Pellegrini, S.; Montemor, M.F. Sulfate-induced corrosion of carbon steel reinforcement in fresh calcium sulfoaluminate binders. *Corrosion* **2022**, *78*, 813–824. https://doi.org/10.5006/3910.
14. Permeh, S.; Lau, K.; Duncan, M.; Simmons, R. Initiation of localized steel corrosion in alkaline sulfate solution. *Mater. Struct.* **2021**, *54*, 143. https://doi.org/10.1617/s11527-021-01740-8.
15. Mundra, S.; Provis, J.L. Mechanisms of passivation and chloride-induced corrosion of mild steel in sulfide-containing alkaline solutions. *J. Mater. Sci*. **2021**, *56*, 14783–14802. https://doi.org/10.1007/s10853-021-06237-x.

16. Nong, Y.; Chen, Z.; Yi, C.; Wang, Y. New insight into the chloride-induced depassivation of steel bar in concrete pore solution: The retarding role of calcium component in passive film. *Constr. Build. Mater*. **2025**, *502*, 144338. https://doi.org/10.1016/j.conbuildmat.2025.144338.
17. Wang, B.; Zhao, Y.; Zhao, L.; Yan, R.; Liu, L.; Cheng, X.; Li, X. Cr-induced enhancement of pitting resistance and passive film stability in alkaline chloride solutions: From electronic properties to pit morphology. *J. Mater. Res. Technol*. **2026**, *41*, 6673–6687. https://doi.org/10.1016/j.jmrt.2026.02.175.
18. Jiang, H.; Jin, Z.; Chen, Y.; Liu, Y.; Zhang, X. The influence of passivation temperature on the corrosion resistance of passivation film for Q235 steel in simulated pore solution of concrete with chloride or/and sulfate ions. *J. Sustain. Cem.-Based Mater*. **2024**, *13*, 1362–1375. https://doi.org/10.1080/21650373.2024.2383927.
19. Jee, A.A.; Pradhan, B. Effect of combined chloride-sulfate solutions and associated cation types with sulfate ions on corrosion performance of steel rebar in concrete. *Adv. Civ. Eng. Mater*. **2022**, *11*, 175–203. https://doi.org/10.1520/ACEM20210121.
20. Hu, Q.; Song, Z.; Xu, Q.; Huang, X.; Chen, S.; Hu, K.; Qian, Q.; Liu, H.; Li, N. Study on the effect of pH on electrochemical corrosion behavior, passive film formation kinetics and structure of 2507 stainless steel in simulated concrete pore solution without chloride ion. *Constr. Build. Mater*. **2026**, *539*, 147427. https://doi.org/10.1016/j.conbuildmat.2026.147427.
21. Liu, Y.; Xin, Q.; Du, Z.; Li, J. pH-sensitive destabilization behavior of passive films on HRB400 steel in low-carbon ferrite-aluminate cement pore solution. *Buildings* **2026**, *16*, 2702. https://doi.org/10.3390/buildings16132702.
22. Liu, C.; Gong, K.; Wei, W.; Wang, Y.; Xie, H.; Mao, F. Coupling influence of pH and Cl^- on the corrosion evolution of passivated Q355B steel in simulated concrete pore solution. *Langmuir* **2025**, *41*, 2458–2470. https://doi.org/10.1021/acs.langmuir.4c04172.
23. Wang, L.; Mercier, D.; Seyeux, A.; Zanna, S.; Maurice, V.; Marcus, P. Investigation of the role of the passive film in the critical pitting temperature of 316L stainless steel by ToF-SIMS and XPS. *Corros. Sci*. **2026**, *264*, 113785. https://doi.org/10.1016/j.corsci.2026.113785.
24. Song, Z.; Zhang, Y.; Liu, L.; Pu, Q.; Jiang, L.; Chu, H.; Luo, Y.; Liu, Q.; Cai, H. Use of XPS for quantitative evaluation of tensile-stress-induced degradation of passive film on carbon steel in simulated concrete pore solution. *Constr. Build. Mater*. **2021**, *274*, 121779. https://doi.org/10.1016/j.conbuildmat.2020.121779.
25. Wan, H.; Wang, Y.; Zhao, Y. In-situ Raman spectroelectrochemistry for characterization of steel corrosion products in simulated concrete pore solution. *J. Build. Eng*. **2025**, *111*, 113098. https://doi.org/10.1016/j.jobe.2025.113098.
26. Li, G.; Evitts, R.; Boulfiza, M. On the corrosion parameters acquired through potentiodynamic scans of carbon steel rebar in simulated pore solution and mortar. *Constr. Build. Mater*. **2023**, *409*, 134160. https://doi.org/10.1016/j.conbuildmat.2023.134160.
27. Alexander, C.L. Electrochemical impedance spectroscopy for corrosion diagnosis of reinforced concrete. *Curr. Opin. Electrochem*. **2026**, *55*, 101790. https://doi.org/10.1016/j.coelec.2025.101790.
28. Alexander, C.L.; Agbakansi, S.C.; De Carvalho Bezerra, W.V.D. Addressing geometric influences on electrochemical impedance spectroscopy for accurate corrosion assessment in steel-reinforced concrete beams. *Corros. Sci*. **2025**, *247*, 112703. https://doi.org/10.1016/j.corsci.2025.112703.
29. Díaz, B.; Nóvoa, X.R.; Pérez, C.; Pintos, A.; Vivier, V. Two- and four-electrode configurations for contactless reinforced concrete corrosion monitoring. *Corrosion* **2023**, *79*, 419–425. https://doi.org/10.5006/4200.
30. Yilmaz, D.; Thoma, K.; Angst, U. A probabilistic framework for modeling chloride-induced corrosion and related load-deformation behaviour of reinforced concrete. *Struct. Concr*. **2026**, 1–20. https://doi.org/10.1002/suco.70776.
31. Shao, W.; He, X.; Shi, D. Durability life prediction of RC piles subjected to localized corrosion in chloride environments. *Eng. Fail. Anal*. **2022**, *136*, 106184. https://doi.org/10.1016/j.engfailanal.2022.106184.
32. Liu, Y.; Li, W.; Guan, J.; Zhou, X.; Guo, L. Multi-field FEM-PD model for non-uniform corrosion and damage evolution in reinforced concrete under chloride-sulfate attack. *Eng. Anal. Bound. Elem*. **2025**, *179*, 106386. https://doi.org/10.1016/j.enganabound.2025.106386.
33. Ejbouh, A.; Ech-Chebab, A.; Hassi, S.; Galai, M.; Benqlilou, H.; Touhami, M.E. Durability assessment of LC3-based reinforced concrete under combined chloride-sulfate environment via the EIS technique. *Constr. Build. Mater*. **2023**, *366*, 130194. https://doi.org/10.1016/j.conbuildmat.2022.130194.
34. Feng, X.; Zhang, Y.; Wu, T.; Zhao, Y.; Wu, T.; Lu, X. A new model for the chloride threshold of carbon steel reinforcement in pore solution under alternating temperatures. Anti-Corros. *Methods Mater*. **2026**, 1–10. https://doi.org/10.1108/ACMM-10-2025-3429.
35. Li, C.; Liu, G.; Fang, Y.; Zhang, Y. Further discussion on the correlation between the corrosion potential and the polarization resistance of steel reinforcement. *Mater. Rep*. **2025**, *39*, 59–64. (In Chinese)

36. Hess, L.; François, R.; Boutillon, L.; Linger, L. Fracture of the passive film on reinforcing steel in concrete under mechanical loading. *Mater. Corros*. **2026**, *77*, 1483–1499. https://doi.org/10.1002/maco.70173.
37. Chen, Z.; Koleva, D. Corrosion behavior of reinforcing steel undergoing stray current and anodic polarization. *Materials* **2021**, *14*, 261. https://doi.org/10.3390/ma14020261.
38. Andrade, C.; Alonso, C. Test methods for on-site corrosion rate measurement of steel reinforcement in concrete by means of the polarization resistance method. *Mater. Struct*. **2004**, *37*, 623–643. https://doi.org/10.1007/BF02483292.
39. RILEM TC 154-EMC. Recommendations of RILEM TC 154-EMC: Electrochemical techniques for measuring metallic corrosion: Half-cell potential measurements, potential mapping on reinforced concrete structures. *Mater. Struct*. **2003**, *36*, 461–471. https://doi.org/10.1617/13718.
40. Orazem, M.E.; Tribollet, B. *Electrochemical Impedance Spectroscopy*, 2nd ed.; Wiley: Hoboken, NJ, USA, 2017.
41. Walter, G.W. A review of impedance plot methods used for corrosion performance analysis of painted metals. *Corros. Sci*. **1986**, *26*, 681–703. https://doi.org/10.1016/0010-938X(86)90033-8.
42. Birnin-Yauri, U.A.; Glasser, F.P. Friedel's salt, $Ca_2Al(OH)_6(Cl,OH)\cdot 2H_2O$: Its solid solutions and their role in chloride binding. *Cem. Concr. Res.* **1998**, *28*, 1713–1723. https://doi.org/10.1016/S0008-8846(98)00162-8.
43. Tang, L.; Nilsson, L.-O. Chloride binding capacity and binding isotherms of OPC pastes and mortars. *Cem. Concr. Res.* **1993**, *23*, 247–253. https://doi.org/10.1016/0008-8846(93)90089-R.
44. Paul, K.W.; Kubicki, J.D.; Sparks, D.L. Sulphate adsorption at the Fe (hydr)oxide–H_2O interface: Comparison of cluster and periodic slab DFT predictions. *Eur. J. Soil Sci*. **2007**, *58*, 978–988. https://doi.org/10.1111/j.1365-2389.2007.00936.x.
45. Liu, G.; Shen, F.; Zhang, Y.; Liu, C.; Yang, L.; Chang, H. Reactive molecular dynamics study on carbon steel corrosion induced by chloride: Effects of applied potential and temperature. *Constr. Build. Mater*. **2024**, *411*, 134250. https://doi.org/10.1016/j.conbuildmat.2023.134250.
46. Klein, N.; Gómez, E.D.; Duffo, G.S.; Farina, S.B. Effect of sulphate on the corrosion of reinforcing steel in concrete. *Constr. Build. Mater*. **2022**, *354*, 129214. https://doi.org/10.1016/j.conbuildmat.2022.129214.
47. Liu, T.; Chen, T.; Zhou, X.; Sun, L.; Yang, W.; Liu, C.; Cheng, X.; Li, X. Investigation of Cr and rare earth (RE) on the corrosion resistance of HRB400 rebar in simulated concrete pore solutions containing chloride and sulfate ions. *Constr. Build. Mater*. **2024**, *423*, 135935. https://doi.org/10.1016/j.conbuildmat.2024.135935.
48. Liu, G.; Li, J.; Zhang, Y. Corrosion of carbon steels subjected to chloride and sulfate in simulated concrete pore solutions with different pH. *Constr. Build. Mater*. **2024**, *440*, 137445. https://doi.org/10.1016/j.conbuildmat.2024.137445.

Disclaimer/Publisher's Note: The statements, opinions and data contained in all publications are solely those of the individual author(s) and contributor(s) and not of MDPI and/or the editor(s). MDPI and/or the editor(s) disclaim responsibility for any injury to people or property resulting from any ideas, methods, instructions or products referred to in the content.